

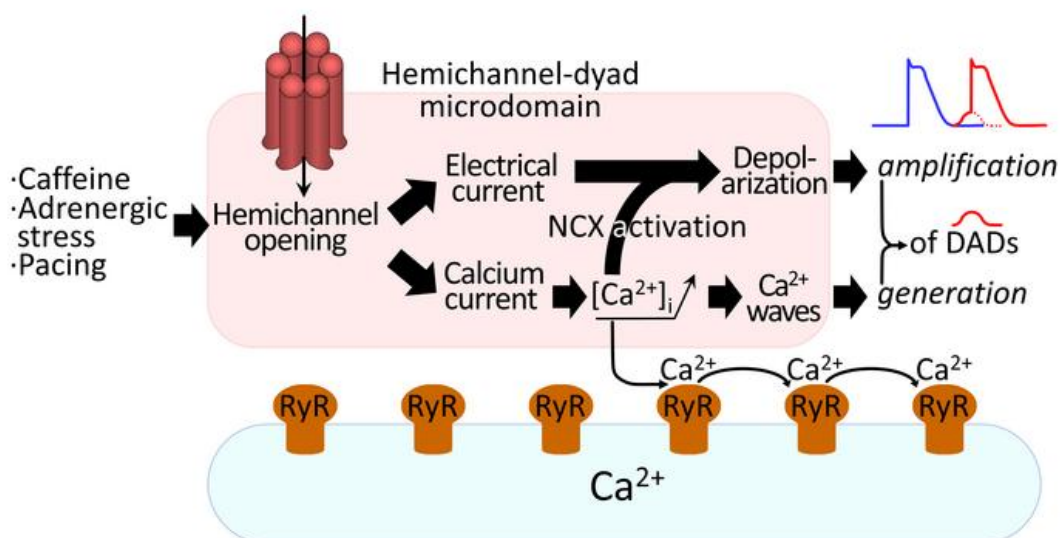
Cx43 hemichannel microdomain signaling at the intercalated disc enhances cardiac excitability

Maarten A.J. De Smet, ... , Karin R. Sipido, Luc Leybaert

J Clin Invest. 2021. <https://doi.org/10.1172/JCI137752>.

Research In-Press Preview Cardiology Cell biology

Graphical abstract



Find the latest version:

<https://jci.me/137752/pdf>



Cx43 hemichannel microdomain signaling at the intercalated disc enhances cardiac excitability

Maarten A. J. De Smet, MD^{1,2,3}, Alessio Lissoni¹, Timur Nezlobinsky^{4,5}, Nan Wang, PhD¹, Eef Dries, PhD², Marta Pérez-Hernández, PhD⁶, Xianming Lin, PhD⁶, Matthew Amoni, MD², Tim Vervliet, PhD⁷, Katja Witschas, PhD¹, Eli Rothenberg, PhD⁸, Geert Bultynck, PhD⁷, Rainer Schulz, MD, PhD⁹, Alexander V. Panfilov, PhD^{4,5,10}, Mario Delmar, MD, PhD^{6}, Karin R. Sipido, MD, PhD^{2*}, Luc Leybaert, MD, PhD^{1*}*

¹Physiology group, Department of Basic and Applied Medical Sciences, Ghent University, Belgium

²Experimental Cardiology, Department of Cardiovascular Sciences, KU Leuven, Belgium

³Department of Internal Medicine, Ghent University, Belgium

⁴Department of Physics and Astronomy, Ghent University, Belgium

⁵Laboratory of Computational Biology and Medicine, Ural Federal University, Ekaterinburg, Russia

⁶Leon H. Charney Division of Cardiology, School of Medicine, New York University, USA

⁷Laboratory of Molecular and Cellular Signaling, Department of Cellular and Molecular Medicine, KU Leuven, Belgium

⁸Department of Biochemistry and Molecular Pharmacology, School of Medicine, New York University, USA

⁹Physiologisches Institut, Justus-Liebig-Universität, Giessen, Germany

¹⁰Arrhythmia Department, Almazov National Medical Research Centre, Saint Petersburg, Russia

*These authors share senior authorship.

Total word count: 10420

Corresponding author:

Luc Leybaert, MD, PhD

Physiology group, Department of Basic and Applied Medical Sciences

Ghent University

Campus UZ Gent Block B, 3rd floor

Corneel Heymanslaan 10

B-9000 Ghent

Belgium

Tel. +32-9-3323366

FAX +32-9-3323059

e-mail Luc.Leybaert@UGent.be

Conflict of Interest

The authors have declared that no conflict of interest exists.

1 **Abstract**

2 Cx43, a major cardiac connexin, forms precursor hemichannels that accrue at the
3 intercalated disc to assemble as gap junctions. While gap junctions are crucial for
4 electrical conduction in the heart, little is known on potential roles of hemichannels. Recent
5 evidence suggests that inhibiting Cx43 hemichannel opening with Gap19 has
6 antiarrhythmic effects. Here, we used multiple electrophysiology, imaging and super-
7 resolution techniques to understand and define the conditions underlying Cx43
8 hemichannel activation in ventricular cardiomyocytes, their contribution to diastolic
9 Ca^{2+} release from the sarcoplasmic reticulum, and their impact on electrical stability. We
10 showed that Cx43 hemichannels are activated during diastolic Ca^{2+} release
11 in single ventricular cardiomyocytes and cardiomyocyte cell pairs from mouse and pig.
12 This activation involved Cx43 hemichannel Ca^{2+} entry and coupling to Ca^{2+} release
13 microdomains at the intercalated disc resulting in enhanced Ca^{2+} dynamics. Hemichannel
14 opening furthermore contributed to delayed afterdepolarizations and triggered action
15 potentials. In single cardiomyocytes, cardiomyocyte cell pairs and arterially perfused
16 tissue wedges from failing human hearts, increased hemichannel activity contributed to
17 electrical instability as compared to non-failing rejected donor hearts. We conclude that
18 microdomain coupling between Cx43 hemichannels and Ca^{2+} release is a novel,
19 targetable, mechanism of cardiac arrhythmogenesis in heart failure.

20 Introduction

21 The pumping function of the heart is coordinated by electrical waves of excitation
22 propagating through the myocardium and initiating cardiac contraction. Propagation of
23 action potentials (APs) between cardiomyocytes is coordinated by gap junctions (GJs)
24 that accrete at the intercalated discs (IDs). Each GJ channel consists of two apposed
25 hemichannels and each hemichannel is further composed of six connexin (Cx) subunits;
26 Cx43 is the predominant Cx isotype in adult heart ventricles (1). GJs organize as channel
27 plaques, called the 'nexus', at the IDs of adjacent cardiomyocytes, which are peripherally
28 surrounded by perinexal zones where unapposed (free) hemichannels reside (2); at rest,
29 GJs are open and hemichannels are closed. In ventricular cardiomyocytes, Cx43
30 hemichannels need strongly positive membrane voltages ($V_m > +50$ mV) to open; the
31 activation threshold is lowered when the cytoplasmic Ca^{2+} concentration ($[Ca^{2+}]_i$) is
32 moderately increased (200-500 nM range), bringing the threshold in the +30 mV range,
33 which may be attained during the peak and plateau phase of the cardiac action potential
34 (3, 4). When open, hemichannels form a large conductance (~220 pS for a single Cx43
35 hemichannel) and poorly selective ion channel and transmembrane conduit with a
36 molecular weight cutoff of ~1.5 kDa (3-9) that allows the passage of various small
37 molecules such as ATP, and ions such as Na^+ , K^+ and Ca^{2+} .

38
39 Inspired by findings in non-cardiac cells where Cx43 hemichannels open in response to
40 moderate $[Ca^{2+}]_i$ elevation at resting V_m (7, 9), we were interested whether Cx43
41 hemichannels in cardiomyocytes could open during sarcoplasmic reticulum (SR) Ca^{2+}
42 release under conditions of Ca^{2+} overload and disease. Cardiomyocytes display
43 synchronized transient $[Ca^{2+}]_i$ elevations during systole, sparked by Ca^{2+} entry through L-

44 type Ca^{2+} channels during the AP plateau, which triggers Ca^{2+} -induced SR Ca^{2+} release
45 via ryanodine receptors (RyRs) (10). Under pathological conditions, spontaneous SR Ca^{2+}
46 release may occur, leading to delayed afterdepolarizations (DADs) during diastole as a
47 result of Ca^{2+} extrusion via the electrogenic $\text{Na}^+/\text{Ca}^{2+}$ exchanger (NCX) that generates
48 depolarizing inward current (11, 12). DADs in turn may lead to disturbances of heart
49 rhythm (12, 13). We hypothesized that hemichannel-associated Ca^{2+} entry as well as
50 hemichannel depolarizing current could enhance DADs. Recent work based on
51 pharmacological inhibition of Cx43 hemichannel opening with Gap19, which renders
52 hemichannels non-available for opening without inhibiting gap junctions (4, 14), has
53 demonstrated antiarrhythmic effects in muscular dystrophy in mice (15, 16), prevention of
54 atrial fibrillation in myosin light chain 4 (MYL4)-related atrial cardiomyopathy (17) and
55 protective effects on disturbed intracellular Ca^{2+} homeostasis in plakophilin-2 (PKP2-)
56 deficient mice, a model of arrhythmogenic right ventricular cardiomyopathy (18).

57
58 We mimicked pathological spontaneous Ca^{2+} release by challenging freshly isolated
59 single ventricular cardiomyocytes and cardiomyocyte cell pairs from mice and pig with
60 caffeine under controlled conditions. Activation of Cx43 hemichannels resulted from
61 microdomain coupling of Cx43 hemichannels to RyRs and SR Ca^{2+} release. We further
62 found that Cx43 hemichannels contribute to spontaneous Ca^{2+} release events and
63 accompanying afterdepolarizations during adrenergic stimulation. In a next translational
64 step, we studied single human ventricular cardiomyocytes and cardiomyocyte cell pairs
65 obtained from heart failure patients, and found that Cx43 hemichannel opening,
66 spontaneous Ca^{2+} release and afterdepolarizations were increased compared to
67 cardiomyocytes from non-failing donor hearts. In arterially perfused tissue wedges,

68 adrenergic stimulation increased the occurrence of DADs and triggered APs, which was
69 clearly more pronounced in wedges from heart failure patients than from non-failing
70 control hearts, and was suppressed by TAT-Gap19 hemichannel inhibition. Collectively,
71 these data show that Cx43 hemichannels become more active in end-stage heart failure
72 and contribute to arrhythmogenic triggered activities in disease, which can be suppressed
73 by TAT-Gap19.

74 **Results**

75 **Ca²⁺ release from the sarcoplasmic reticulum at resting membrane potentials**
76 **activates Cx43 hemichannels**

77 Freshly isolated left ventricular cardiomyocytes from mouse and pig hearts were voltage
78 clamped at -70 mV, under physiological extracellular Ca²⁺ concentrations and continuous
79 [Ca²⁺]_i monitoring with fluo-4 (50 μmol/L), and subjected to a two-pulse caffeine stimulation
80 protocol (Figure 1A). Caffeine stimulation (10 mmol/L) created controlled conditions of SR
81 Ca²⁺ release, mimicking the spontaneous release observed in pathological conditions.
82 Caffeine activates ryanodine receptors (19) and triggers transient SR Ca²⁺ release with
83 resulting forward-mode inward NCX current (10, 20). In line with this, the first caffeine
84 pulse triggered a [Ca²⁺]_i transient and resulting NCX current; by contrast, the second
85 caffeine pulse was not accompanied by [Ca²⁺]_i elevation and NCX current, indicating Ca²⁺
86 store depletion (Figure 1B). Superimposed on the macroscopic NCX current during the
87 first caffeine pulse, microscopic unitary current events appeared in a Ca²⁺ release-
88 dependent manner (Supplemental Figure 2B). Such events were absent during the
89 second caffeine pulse and were abolished by including the Ca²⁺ chelator BAPTA (10
90 mmol/L) in the pipette (Figure 1 C-E and Supplemental Figure 3). Additionally, imposing
91 stably buffered [Ca²⁺]_i did not induce unitary currents, indicating that unitary current activity
92 is dependent on SR Ca²⁺ release rather than on caffeine or [Ca²⁺]_i elevation itself
93 (Supplemental Figure 4) as previously noted (21). Since Ca²⁺ release in cardiomyocytes
94 is not homogeneous but characterized by differences in bulk cytoplasmic and
95 subsarcolemmal [Ca²⁺]_i (22), we probed the involvement of [Ca²⁺]_i microdomains in unitary
96 current activation by plotting ensemble current versus subsarcolemmal [Ca²⁺]_i as derived
97 from the NCX current (23) (Supplemental Figure 2C). Ensemble currents showed no

98 hysteresis in a low $[Ca^{2+}]_i$ range of NCX-derived subsarcolemmal measurements, but
99 hysteresis became apparent at higher concentrations resulting from hemichannel closure
100 at high $[Ca^{2+}]_i$ (21).

101
102 Unitary events in response to SR Ca^{2+} release could be readily observed in ~96% of
103 mouse myocytes and ~60% of pig myocytes with a representative event count of ~38 and
104 ~6 respectively over the 8 s recording window (Supplemental Table 6). Most unitary
105 current activity occurred within less than 100 ms after the start of the NCX current and
106 had a ~220 pS unitary conductance in both species (Figure 1C-E), typical for Cx43
107 hemichannel opening (3, 4, 6). A ~110 pS substate could also be resolved, especially in
108 pig. Occasionally, we observed 'stacked' opening events with a conductance of multiples
109 of ~220 pS (Figure 1C-E). Stepping V_m to different voltages during caffeine application,
110 under conditions of K^+ -channel blockade, allowed us to construct IV plots with a slope
111 conductance of ~220 pS and reversal potential ~0 mV for both species (Figure 1F-G). The
112 zero reversal potential is a typical property of poorly selective Cx hemichannels.
113 Increasing extracellular Ca^{2+} 5-fold significantly increased the slope conductance and
114 shifted the reversal potential rightward in the direction of the increased Nernst potential
115 for Ca^{2+} , indicating substantial Ca^{2+} flow through the channel (Figure 1G). When a caffeine
116 challenge was given at positive V_m instead of -70 mV, the short ~8 ms unitary opening
117 events attained a strongly prolonged character (100 – 120x increase in open time),
118 resembling the long duration hemichannel openings observed previously (3, 4, 6) (Figure
119 1F and Supplemental Figure 2D). Unitary current properties and interspecies differences
120 are summarized in Supplemental Table 6.

121

122 To confirm the Cx43 hemichannel origin of the Ca²⁺ release-induced unitary currents, we
123 used a combination of pharmacological and genetic approaches targeting Cx43 (Figure
124 1H-I). Cx43 knockdown by ~80% (Supplemental Figure 5A-D) strongly and significantly
125 reduced unitary current activities. We additionally tested a set of Cx43 targeting peptides
126 that interfere with hemichannel function (Figure 1H-I and Supplemental Figure 6A; peptide
127 administration and concentrations see Methods). Gap19 significantly reduced unitary
128 current activities while the inactive mutant (4), Gap19^{I130A}, had no effect. Conversely, the
129 hemichannel opening enhancer CT9 (5, 24) significantly increased unitary currents. We
130 screened for other channels with a similar biophysical profile such as Panx1, TRPP2 and
131 TRPP5 (25, 26). Firstly, ventricular Panx1 and TRPP2/5 protein levels were unchanged
132 or undetected in Cx43^{Cre-ER(T)/fl} ventricles (Supplemental Figure 5E-H). Additionally, the
133 pannexin-1 targeting peptide ¹⁰Panx1 did not affect unitary currents (Figure 1I). None of
134 the peptides or experimental conditions affected SR Ca²⁺ content as determined by
135 integrating the NCX current during caffeine superfusion (Supplemental Figure 6B).

136

137 **Cx43 hemichannel opening is modulated by stimulation frequency and enhanced**
138 **during β-adrenergic stimulation**

139 It is well known that cardiomyocyte responses to repeated electrical stimulation or β-
140 adrenergic stimulation occur in part through alterations in [Ca²⁺]_i signaling and SR Ca²⁺
141 content (20). We thus verified whether Cx43 hemichannel activity was influenced by
142 increasing stimulation frequency and β-adrenergic activation. Ca²⁺ release-induced
143 unitary current activity significantly and reversibly increased when increasing the
144 stimulation frequency before caffeine application (0.5 to 4 Hz range in mouse and 0.5 to
145 2 Hz range in pig) (Figure 2A-D). The increase was proportional to changes in the

146 amplitude of the caffeine-induced SR Ca^{2+} release (Figure 2E-F). Moreover, β -adrenergic
147 stimulation by superfusion of isoproterenol (ISO) during the 2 min train at 1 Hz significantly
148 increased unitary current activities (Figure 3A-D), in line with concurrent changes in SR
149 Ca^{2+} content (Figure 3E).

150
151 **Cx43 associates with dyads at the intercalated disc where microdomain activation**
152 **of Cx43 hemichannels occurs**

153 Since Cx43 hemichannels are activated by a subsarcolemmal increase in Ca^{2+} during
154 caffeine-induced SR Ca^{2+} discharge, we hypothesized that these channels would
155 intimately associate with cardiac dyads at the ID. We used single-molecule light
156 microscopy (SMLM) by performing stochastic optical reconstruction microscopy
157 (STORM) to map Cx43 distribution to dyadic nanodomains in single cardiomyocytes and
158 cardiomyocyte cell pairs from mouse left ventricle. We first used immunolabeling of Cx43
159 in combination with an SR marker (RyR2, Junctophilin-2 (JPH2) or total Phospholamban
160 (tPLN)) or a sarcolemmal membrane marker (pore-forming subunit of the L-type Ca^{2+}
161 channel (Cav1.2), NCX or Caveolin-3 (Cav3)). All markers showed the largest cluster
162 density and cluster size at the cell ends of single cardiomyocytes and at the IDs of
163 cardiomyocyte cell pairs as compared to the lateral surface or cell interior (Supplemental
164 Figure 7A-C). By contrast, the Z-disc protein α -actinin - used as a negative control - did
165 not follow such distribution and showed highest cluster density and size in the cell interior
166 (Supplemental Figure 7C). Distance analysis revealed that 30-50 % of the studied markers
167 occurred within ~20 nm of Cx43 at the cell ends of single cardiomyocytes or at the IDs of
168 cardiomyocyte cell pairs (Supplemental Figure 7D). To exclude random association of
169 Cx43 to these overtly abundant markers, we performed stochastic simulations on these

170 data to determine the interaction factor, which expresses the relation of the
171 experimentally observed overlap versus the probability for random overlap (Interaction
172 factor ImageJ plugin (27)). Cx43 co-localized to all markers with an interaction factor >
173 0.6, indicating that the observed overlap is deterministic rather than random
174 (Supplemental Figure 7E-F).

175
176 We used a triple staining of Cav1.2, RyR2 and Cx43 to directly map the relation of Cx43
177 to dyads (based on Cav1.2 and RyR2 clusters occurring < 250 nm of each other (28, 29))
178 (Figure 4A-B). We found that ~80% of RyR2 associated in dyads and that dyadic RyR2
179 clusters were larger than their extradyadic counterparts. Both dyadic and extradyadic
180 RyR2 cluster densities and number of molecules were largest at the cell ends of single
181 cardiomyocytes and at the IDs of cardiomyocyte cell pairs as compared to the lateral
182 surface or cell interior (Figure 4C). Only a small fraction of extradyadic RyR2 clusters
183 occurred within ~20 nm of Cx43 while ~50% of dyadic RyR2 co-localized with Cx43
184 (Figure 4C). Recent work has shown that closely localized RyR clusters, < 100 nm edge-
185 to-edge distance, may act cooperatively as superclusters to generate Ca²⁺ signals (30).
186 These RyR superclusters preferentially organized in dyads and occurred more frequently
187 at the cell ends of single cardiomyocytes and at the IDs of cardiomyocyte cell pairs as
188 compared to the lateral surface or cell interior (Figure 4D). Superclusters at these sites
189 contained more RyRs (Figure 4D). Overall, dyadic superclusters formed the majority of
190 structures that co-localized with Cx43.

191
192 Next, we used a relative localization algorithm (31, 32) to categorize dyadic Cav1.2
193 clusters at the IDs of cardiomyocyte cell pairs as either located in the perinexus (based

194 on the signal overlapping with Cx43 and extending within 200 nm of Cx43 clusters) or
195 distant from Cx43 (based on signal extending beyond 200 nm of Cx43 clusters). We found
196 that ~80% of Cav1.2 clusters occurred in dyads; approximately 42% of these clusters
197 overlapped with Cx43 and another ~28% occurred adjacent to Cx43, resulting in ~70% of
198 dyads at the ID occurring in the perinexal nanodomain where Cx43 hemichannels are
199 known to reside (Figure 4E and Supplemental Figure 8A). Cx43 and dyadic Cav1.2
200 clusters overlapped only partially, confirming association at the edge of Cx43 clusters
201 (Supplemental Figure 8B). In line with these observations, electron microscopy of murine
202 cardiac ventricular tissue revealed cleft formation of SR cisterns with the perinexal
203 nanodomain where Cx43 hemichannels reside (Figure 4F, Supplemental Video 1 and 2)
204 (33, 34). Based on the protein structure of Cx43 channels (35), the distance to nearest
205 neighbor in cardiac GJ plaques (36) and the lower density of Cx43 in the perinexus (37),
206 we calculated that perinexal dyads or dyads at the cell end may contain 1-2 Cx43
207 hemichannels per dyad (Supplemental Figure 9).

208
209 To provide a functional correlate to these structural observations, we used the macropatch
210 technique (38) to map single Cx43 hemichannel activity at discrete sarcolemmal
211 microdomains. During caffeine-induced SR Ca²⁺ release, we observed single-channel
212 currents with a conductance of ~220 pS at the cell ends of single cardiomyocytes and IDs
213 of cardiomyocyte cell pairs. One third of patches at these sites had currents, with currents
214 being absent in lateral membranes (Figure 5A-D, Supplemental Table 7). Open probability
215 was highest in cardiomyocyte cell pairs. Events were inhibited by TAT-Gap19, enhanced
216 by TAT-CT9 and abolished in cells not expressing Cx43. ¹⁰Panx1 and inactive TAT-
217 Gap19^{130A} had no effect (Figure 5D). We used scanning ion conductance microscopy

218 (SICM) to map membrane topology at the cell end and recorded ~220 pS caffeine-induced
219 unitary current activity (including ~110 pS substate) in nanopatches (R_p ~30 M Ω , ~300
220 nm pipette internal diameter) just distally of t-tubules at the start of the ID (Figure 5E-G).
221 Patches contained 1-2 active channels, in line with our predictions (Supplemental Figure
222 9 and Supplemental Table 7).

223
224 **Cx43 hemichannels modulate diastolic Ca²⁺ release during adrenergic stimulation**
225 **and associated arrhythmogenic afterdepolarizations**

226 Since highly conductive and Ca²⁺ permeable hemichannels are localized near dyads at
227 the ID, it is conceivable that they could contribute to diastolic SR Ca²⁺ release itself (11).
228 To investigate this, we exposed the cardiomyocytes to fast pacing and β -adrenergic
229 stimulation without caffeine, and recorded spontaneous SR Ca²⁺ release events and
230 currents occurring after such stimulation (Figure 6A). Additionally, we monitored V_m
231 changes after switching to current clamp conditions following the same stimulation
232 protocol (Figure 6B). Compared to baseline, diastolic Ca²⁺ release, accompanying
233 currents and afterdepolarizations became prominent following fast pacing and ISO
234 exposure (Figure 6C). Gap19 and Cx43 knockdown reduced the number of diastolic Ca²⁺
235 release events and associated currents while CT9 enhanced these events, Gap19^{I130A}
236 had no effect (Figure 6D). Accordingly, DADs and triggered APs following a period of fast
237 pacing and ISO stimulation (Figure 6B-C), were significantly reduced by TAT-Gap19, not
238 affected by TAT-Gap19^{I130A} and enhanced by TAT-CT9 (Figure 6D).

239
240 We verified whether the Cx43 targeting peptides or Cx43 knockdown would perhaps affect
241 the properties of the global [Ca²⁺]_i transient. This was not the case, indicating absence of

242 gross effects of these interventions on cardiomyocyte global Ca^{2+} homeostasis
243 (Supplemental Figure 10). In a next approach, we further scrutinized the occurrence of
244 hemichannel activity following adrenergic stimulation in the time window of macroscopic
245 NCX currents associated with spontaneous Ca^{2+} release. We found that ~ 220 pS unitary
246 current events occurred not only during the NCX current (superimposed on it, see Figure
247 7A) but also preceding it (Figure 8A; corresponding conductance histograms are shown
248 in Figure 7B and 8B respectively). Event probabilities before and during NCX were
249 comparable (compare Figure 7C with 8C) and strongly increased by pacing and ISO.
250 Unitary current activity during adrenergic stimulation was robustly associated with larger
251 Ca^{2+} transients, larger SR Ca^{2+} content and increased spontaneous Ca^{2+} release
252 (Supplemental Figure 11). Genetic ablation and pharmacological tools had effects as
253 observed in the caffeine-triggered responses (Figure 7D and 8D; compare to Figure 1I).
254 As expected, charge transfer associated with these unitary hemichannel events was
255 significantly smaller compared to charge transfer linked to the NCX current during
256 spontaneous Ca^{2+} release (Figure 7E).

257
258 As a control experiment, we tested whether Gap19, CT9 and their TAT-versions affected
259 Ca^{2+} release via RyR2. To this end, we challenged RyR2 overexpressing HEK293 cells
260 (39) with caffeine and quantified Ca^{2+} signals in the presence or absence of peptide.
261 Overall, peptides did not influence caffeine-induced Ca^{2+} signals, except for acute TAT-
262 CT9 exposure which significantly increased Ca^{2+} release at 5 mM caffeine but not at 0.4
263 mM; no effect was observed when TAT-CT9 was pre-incubated (Supplemental Figure 12).

264

265 **Cx43 hemichannel depolarizing current, microdomain Ca²⁺ entry and RyR-coupling**
266 **underlie hemichannel associated triggered activities**

267 To better understand these observations, we performed order of magnitude calculations
268 within a mathematical framework (see supplemental information) incorporating the
269 present unitary current and STORM imaging data. We reasoned that open hemichannels
270 pass inward current and facilitate Ca²⁺ entry into the cell. The direct contribution of
271 depolarizing current through a single hemichannel was determined to be ~1.6 mV (at -70
272 mV and 37°C; Figure 9A). We further estimated the hemichannel Ca²⁺ current to be ~0.84
273 and ~1.46 pA for 1.0 (mouse) and 1.8 mM (pig and human) extracellular Ca²⁺ respectively,
274 corresponding to a Ca²⁺ entry rate of ~4.35x10⁻¹⁸ and ~7.57x10⁻¹⁸ mol Ca²⁺ per second
275 and per open hemichannel respectively. We calculated that such Ca²⁺ influxes do not
276 impact global cytosolic Ca²⁺ (in line with experimental findings presented in Supplemental
277 Figure 10 (40-44)), but result in a pronounced elevation of peak [Ca²⁺]_i in the hemichannel-
278 dyad microdomain of ~0.81 and ~3.44 μmol/L respectively (Figure 9B, calculations based
279 on a hemichannel open time τ of 8 ms derived from the open time distribution). Such Ca²⁺
280 elevation may activate significant NCX current in the order of 0.12 and 0.13 pA/pF
281 respectively, producing ~1.28 and ~1.51 mV depolarization respectively (Figure 9A and
282 C). Thus, during a DAD, where hemichannel opening probability is largest during peak
283 NCX current (Figure 7F), membrane depolarization will amount to ~2.88 and ~3.11 mV
284 per hemichannel (Figure 9A), which is in line with the experimental observation that TAT-
285 Gap19 decreases DAD amplitude by 2.83 mV (Figure 6D). Conversely, TAT-CT9
286 increased DAD amplitude by 4.9 mV, which may be related to longer opening or
287 occasional stacked hemichannel openings (Figure 6D). Thus, hemichannel opening will

288 increase the DAD peak amplitude, bringing it closer to the threshold for action potential
289 firing.

290
291 We further included a 4-state Markov RyR gating model (45) in the hemichannel-dyad
292 microdomain to estimate the effect of hemichannel Ca^{2+} entry on Ca^{2+} -induced Ca^{2+}
293 release. This suggested that single hemichannel Ca^{2+} entry may activate a RyR
294 supercluster at the cell end with a probability of ~ 0.72 and ~ 0.99 (for 1.0 and 1.8 mM
295 extracellular Ca^{2+} respectively) thus providing a Ca^{2+} spark (Figure 9A). This Ca^{2+} spark
296 at the intercalated disc has a ~ 0.99 probability of activating a neighboring RyR cluster;
297 accordingly Ca^{2+} entry through a single hemichannel has a respective probability of ~ 0.71
298 and ~ 0.98 to induce a propagating Ca^{2+} wave (Figure 9A, D-E) (46). Experimentally, we
299 analyzed coupling of Cx43 hemichannel opening activity to diastolic Ca^{2+} release as well
300 as the relation to the site of origin, in particular at the cell end. This analysis revealed that
301 hemichannel currents preceded $\sim 50\%$ of the spontaneous Ca^{2+} release events following
302 adrenergic stimulation in mice, i.e. somewhat lower than the 71% predicted; this coupling
303 was fast ($\tau \approx 10$ ms) and occurred almost exclusively for waves that started at the cell end
304 (Supplemental Video 4, Figure 8A and E) as compared to the middle (Supplemental Video
305 3, Figure 7A and Figure 8E). Ca^{2+} waves originating from the cell end had a significantly
306 higher amplitude and larger associated NCX currents as compared to those originating in
307 the cell middle (Figure 8F).

308

309 **Cx43 hemichannels affect cardiac excitability in human heart failure**

310 In human heart failure, Cx43 expression and distribution change and we asked the
311 question whether in those conditions, as compared to healthy hearts, Cx43 hemichannels
312 affected cardiac excitability. We examined explanted hearts from patients with end-stage
313 heart failure; non-failing rejected donor hearts were used as controls. Patient
314 characteristics are summarized in Supplemental Table 8. Failing hearts were
315 hypertrophic, dilated and showed severely reduced left ventricular ejection fraction
316 (Supplemental Table 8, Supplemental Figure 13A-B). Concurrently, isolated left
317 ventricular cardiomyocytes from failing hearts were hypertrophied compared to controls
318 (Supplemental Figure 13C-D). In cardiomyocytes from non-failing human left ventricles,
319 caffeine-induced SR Ca²⁺ release evoked ~220 pS unitary current activity superimposed
320 on the NCX current (Figure 10A-C). Unitary events increased with stimulation at higher
321 frequency and were ISO sensitive (Figure 10D-G), as observed in mice and pig (Figure
322 2). Interestingly, these unitary current activities were more frequent in cardiomyocytes
323 from failing hearts, especially during fast pacing and adrenergic stimulation (Figure 10D-
324 I) and were inhibited by Gap19 (Figure 10H-I). In non-failing human cardiomyocytes, ~220
325 pS unitary current activity could only be recorded at the cell ends of single cardiomyocytes
326 or the ID of cardiomyocyte cell pairs, while in failing cardiomyocytes unitary current activity
327 was also recorded at the lateral membrane of single cardiomyocytes and cardiomyocyte
328 cell pairs (Figure 11A-D). In heart failure, patches contained more channels with higher
329 open probability (Figure 11E-F). In non-failing and failing cardiomyocytes, these unitary
330 currents were blocked by subsequent application of TAT-Gap19 (Figure 11D and F).

331
332 Similar to mouse, we observed unitary current activity with ~220 pS unitary conductance
333 preceding and during spontaneous diastolic Ca²⁺ release following adrenergic stimulation

334 (Figure 12A-C), which was inhibited by Gap19. Additionally, we found that Gap19
335 significantly decreased spontaneous Ca^{2+} release and resulting NCX currents in
336 cardiomyocytes from non-failing and failing hearts (Figure 12A, D-E). Current clamp
337 recording revealed significantly increased frequency and amplitude of DADs and triggered
338 APs in failing hearts as compared to non-failing hearts, and these events (induced by fast
339 pacing and ISO stimulation) were significantly reduced by TAT-Gap19 (Figure 12F-G).
340 Finally, monophasic action potential recordings on arterially perfused tissue wedges from
341 failing human hearts showed the highest occurrence of DADs and triggered APs following
342 2 Hz and ISO stimulation as compared to non-failing wedges, which was significantly
343 reduced by TAT-Gap19 (Figure 12H-I). Neither in non-failing nor in failing hearts, did we
344 find gross effects of Gap19 on cardiomyocyte Ca^{2+} transients or SR Ca^{2+} content
345 (Supplemental Figure 14A). Similar to mouse, we found that Cx43 hemichannel opening
346 was related to diastolic Ca^{2+} release originating from the cell end in non-failing
347 cardiomyocytes; most interestingly, in myocytes from failing hearts hemichannel opening
348 occurred more frequently in relation to Ca^{2+} release originating from the cell middle as
349 compared to those isolated from non-failing hearts (Supplemental Figure 14D-E). Gap19
350 attenuated both frequency and amplitude of Cx43 hemichannel-associated Ca^{2+} release
351 and associated NCX currents (Supplemental Figure 14F).

352 **Discussion**

353 Our results demonstrate that Ca²⁺-permeable Cx43 hemichannels can be activated by SR
354 Ca²⁺ release at resting V_m. Microdomain coupling of Cx43 to distinct dyads at the ID
355 facilitates this activation and underlies modulation of local Ca²⁺ release by Cx43 at these
356 sites. Through both these mechanisms, Cx43 hemichannels contribute to triggered
357 activity. Cx43 hemichannels are more active in human heart failure, especially during
358 adrenergic stimulation, and thereby contribute to electrical instability and
359 arrhythmogenesis in heart failure.

360

361 **Molecular identity of the large conductance channel during SR Ca²⁺ release**

362 In 1990, Pott and Mechmann (47) were the first to describe the large conductance channel
363 activated by caffeine-induced or spontaneous SR Ca²⁺ release in guinea pig atrial
364 cardiomyocytes. They argued that these channels were possibly related to “cardiac gap
365 junction hemichannels” based on their biophysical profile and pharmacology. Here, we
366 expand and validate these findings across species, including humans, and demonstrate
367 that Cx43 hemichannels constitute the large conductance channel using genetic and
368 pharmacological tools to complement the biophysical profiling. Over the years, other
369 large-conductance channels expressed in cardiomyocytes have been proposed to
370 underlie the spiking unitary current activities superimposed on the NCX current.
371 Sarcolemmal RyRs have been suggested (48, 49) but our finding that unitary activity
372 disappears upon SR depletion contradicts the possibility of sarcolemmal RyRs. Transient
373 receptor potential (TRP) channel family members such as PKD2 (TRPP2) or PKD2L2
374 (TRPP5) as well as Panx1 channels have also been suggested (25, 26); however, Panx1
375 and TRPP2/5 expression were unchanged upon Cx43 knock down and ¹⁰Panx1 did not

376 influence unitary activity. Instead, the biophysical profile described here, combined with
377 Gap19 hemichannel inhibition and genetic interventions, strongly point to Cx43
378 hemichannels as the responsible large conductance channel.

379
380 Importantly, this is the first study demonstrating that Cx43 hemichannels may be activated
381 by SR Ca^{2+} release in cardiomyocyte cell pairs, where gap junctions are present (50, 51),
382 indicating that functional Cx43 hemichannels are present in ventricular myocardium and
383 are not a byproduct of cell dissociation.

384
385 **Cx43 hemichannels and microdomain Ca^{2+} signaling**

386 Cx43 hemichannel activity was modulated by stimulation frequency and isoproterenol.
387 High frequency and beta-adrenergic stimulation enhance microdomain Ca^{2+} signaling at
388 the dyad (52, 53). Dyads are composed of junctional SR that is juxtaposed to L-type Ca^{2+}
389 channels in T-tubules; EM-based evidence has indicated that junctional SR is also present
390 at the ID (54, 55). Here, we provide structural and functional support for the existence of
391 a Cx43 hemichannel-SR Ca^{2+} release signaling microdomain consisting of large dyadic
392 RyR2 superclusters at the perinexus in healthy myocardium. Cx43 hemichannel opening
393 had no effect on global cellular Ca^{2+} dynamics or SR Ca^{2+} content, indicating that
394 hemichannels do not contribute to canonical excitation-contraction coupling. However, we
395 show that Cx43 hemichannels impact cardiomyocyte electrical excitability by (i) providing
396 direct depolarizing current and (ii) Ca^{2+} entry, increasing NCX current and consequent
397 DAD amplitudes and triggered APs. A third level of impact relates to the finding that Ca^{2+} -
398 permeable hemichannels facilitate and increase diastolic SR Ca^{2+} release, in particular at
399 the ID. Numerical simulations corroborate this and indicate that single hemichannel Ca^{2+}

400 entry into dyads at the ID highly promotes Ca^{2+} -induced Ca^{2+} release from neighboring
401 RyR superclusters followed by propagating Ca^{2+} waves resulting in DADs. Together these
402 observations may explain the previously observed impact of Cx43 hemichannel inhibition
403 on adrenergic arrhythmias in muscular dystrophy (15, 16, 56), ARVC (18) and MYL4
404 mutation-associated atrial fibrillation (17).

405

406 **Cx43 hemichannels as an arrhythmogenic mechanism in human heart failure**

407 In human heart failure, we observed a significant increase in hemichannel activity during
408 SR Ca^{2+} release and adrenergic stimulation. Cx43 hemichannel inhibition significantly
409 reduced adrenergically-mediated diastolic SR Ca^{2+} release and associated DADs and
410 triggered APs at the cellular level as well as in arterially perfused tissue wedges from non-
411 failing and failing human left ventricle. As in mouse, Cx43 hemichannel inhibition had no
412 gross effects on cellular Ca^{2+} signaling or SR Ca^{2+} content in non-failing and failing
413 cardiomyocytes. Yet, hemichannels enhance diastolic SR Ca^{2+} release presumably
414 through microdomain Ca^{2+} signaling. Interestingly, Cx43 events and the coupling to Ca^{2+}
415 were observed at the cell ends as well as in the middle, reflecting a shift in Cx43 location
416 as well as in ryanodine receptor activity (54). Indeed, macropatch recording shows that –
417 in heart failure – hemichannel activity may redistribute from the cell ends to the lateral
418 membranes of single cardiomyocytes and cardiomyocyte cell pairs. Taken together, these
419 data provide evidence that Cx43 hemichannels function as a ventricular arrhythmogenic
420 mechanism that can be targeted by Gap19 without negative impact on inotropy.

421

422 A limitation of this study is that numerical simulations were based on (i) several
423 assumptions and only give an order of magnitude of the effect, and (ii) the functional and

424 structural data were obtained in control cardiomyocytes, not in diseased cells. This may
425 be the reason why the calculated probability of single hemichannel opening leading to
426 Ca^{2+} waves was somewhat higher than observed in the experiments (0.71 vs 0.5).
427 Second, in the human heart experiments, control non-failing cardiomyocytes were
428 obtained from hearts that were not suitable for transplantation for various reasons (e.g.
429 age, comorbidity), implying that these controls may differ from what is considered as
430 healthy.

431 **Methods**

432 We utilized commercially available C57/BL6 mice and healthy control pigs. Additionally,
433 we used an established inducible Cx43 knock-down mouse model (Cx43^{Cre-ER(T)/fl} mice
434 (57-63)). Daily intraperitoneal injection of 3 mg 4-hydroxytamoxifen (4-OHT; Sigma-
435 Aldrich, Bornem, Belgium) dissolved in sunflower oil, for 5 consecutive days, induces Cre-
436 ER(T) activity which progressively deletes the floxed Cx43 allele in adult Cx43^{Cre-ER(T)/fl}
437 mice. Experimental work was performed on day 11 after the first injection. 4-OHT-treated
438 Cx43^{fl/fl} mice were used as controls. Animals were housed in a licensed facility and
439 handled in accordance with European Directive 2010/63/EU. For human studies, we used
440 rejected donor hearts as well as explanted failing hearts. Patient characteristics are
441 summarized in Supplemental Table 8.

442
443 Procedures used for cardiomyocyte isolation, cellular electrophysiology and simultaneous
444 Ca²⁺ imaging in single ventricular cardiomyocytes, DNA extraction, PCR, western blots,
445 confocal and electron and single-molecule localization microscopy, cell culture, siRNA
446 transfection, macropatch and super-resolution patch clamp, monophasic action potential
447 recording in ventricular tissue wedges and numerical simulations follow previously
448 published protocols and are detailed in the Online data supplement.

449
450 Synthetic peptides used in this study to interfere with Cx/Panx channel function were all
451 obtained from Pepnome (Hong Kong, China). Gap19, Gap19^{I130A} and CT9 were added to
452 the pipette solution at a concentration of 100 µmol/L. TAT-Gap19, TAT-Gap19^{I130A} and
453 TAT-CT9 were added to the bath solution at 80 µmol/L. ¹⁰Panx1, a blocker of Panx1
454 channels, was pre-incubated at 200 µmol/L for 30 minutes and present in the extracellular

455 solution during whole cell recording. For macropatch experiments, ¹⁰Panx1 was included
456 in the pipette solution at 200 μmol/L. The identity of the peptides was confirmed by mass
457 spectrometry and purity was ≥ 90 %.

458

459 **Statistics**

460 Data are expressed as mean ± standard error of the mean (SEM) unless otherwise
461 indicated, with 'n' denoting the number of cells and 'N' denoting the number of
462 independent experiments. Following outlier analysis (mean ± 3xSD), normality of
463 distribution was tested and appropriate statistical test was determined for comparative
464 statistics. Data were compared using a nested design taking into account n cells and 'N'
465 animals or human hearts. A two-tailed P value < 0.05 was considered as indicating
466 statistical significance. In the graphs, the actual P values are provided. Statistical analysis
467 and graphical data representation was done with Graphpad Prism (v.9).

468

469 **Study approval**

470 Experimental methods were approved by the local ethical committees of animal research
471 at Ghent University, KU Leuven and New York University School of Medicine.

472

473 For human studies, experimental procedures were approved by the Ethical Committee of
474 the University Hospital of Leuven with permit number S58824; as this is residual tissue no
475 informed consent was necessary.

476 **Author contributions**

477 M.D.S. designed, conducted and analyzed most of the experiments, and wrote and
478 revised the manuscript with input from all the authors. A.L. contributed to experimental
479 design. T.N. designed the software for analysis of membrane currents and numerical
480 simulations. N.W. contributed to the experimental design. E.D. contributed to
481 cardiomyocyte cell isolation and cellular electrophysiology. M.P.H. contributed to the
482 design and analysis of super-resolution and electron microscopy experiments. X.L.
483 performed SICM-guided patch clamp experiments. M.A. contributed to cardiomyocyte cell
484 isolation, cellular electrophysiology and monophasic action potential recording. T.V.
485 performed and analyzed all experiments with tetracycline-inducible RyR2 overexpressing
486 cells. K.W. contributed to single channel analysis. E.R. guided experimental design and
487 provided computational tools for processing and analysis of super-resolution fluorescence
488 microscopy. G.B. guided experiments in tetracycline-inducible RyR2 overexpressing cells.
489 R.S. provided inducible Cx43 knock down mice. A.V.P. guided design of analysis software
490 and numerical simulations. M.D., K.R.S. and L.L. conceived, initiated and supervised the
491 project, gave scientific input and revised the manuscript.

492 **Acknowledgements**

493 We sincerely thank Dr. Ellen Cocquyt, Diego De Baere, Dr. Vicky Pauwelyn, Dr. Annemie
494 Biesemans, Roxane Menten and Dr. Mingliang Zhang for superb technical support. We
495 would also like to thank the heart failure unit, the transplant surgical team and the
496 transplant coordinating team of UZ Leuven for the help in providing the human explant
497 hearts.

498
499 This work was supported by the Fund for Scientific Research Flanders (project grants to
500 L.L., K.R.S. and G.B., a postdoctoral fellowship to E.D. and PhD fellowships to M.D.S.
501 and M.A.), Ghent University (a postdoctoral fellowship to K.W. and PhD fellowships to A.L.
502 and T.N.), the Interuniversity Attraction Poles P7/10 to K.R.S. and L.L., National Institutes
503 of Health (project grants to E.R. and M.D.), the Fondation Leducq (transatlantic network
504 award to M.D.) and a grant from the Ministry of Science and Higher Education of the
505 Russian Federation, agreement 075-15-2020-800, to AVP.

506 **References**

- 507 1. Giovannone S, Remo BF, and Fishman GI. Channeling diversity: Gap junction
508 expression in the heart. *Heart Rhythm*. 2012;9(7):1159-62.
- 509 2. Rhett JM, Veeraraghavan R, Poelzing S, and Gourdie RG. The perinexus: sign-
510 post on the path to a new model of cardiac conduction? *Trends Cardiovasc Med*.
511 2013;23(6):222-8.
- 512 3. Wang N, De Bock M, Antoons G, Gadicherla AK, Bol M, Decrock E, et al.
513 Connexin mimetic peptides inhibit Cx43 hemichannel opening triggered by
514 voltage and intracellular Ca²⁺ elevation. *Basic Res Cardiol*. 2012;107(6):304.
- 515 4. Wang N, De Vuyst E, Ponsaerts R, Boengler K, Palacios-Prado N, Wauman J, et
516 al. Selective inhibition of Cx43 hemichannels by Gap19 and its impact on
517 myocardial ischemia/reperfusion injury. *Basic Res Cardiol*. 2013;108(1):309.
- 518 5. Bol M, Wang N, De Bock M, Wacquier B, Decrock E, Gadicherla A, et al. At the
519 cross-point of connexins, calcium, and ATP: blocking hemichannels inhibits
520 vasoconstriction of rat small mesenteric arteries. *Cardiovasc Res*.
521 2017;113(2):195-206.
- 522 6. Contreras JE, Sáez JC, Bukauskas FF, and Bennett MVL. Gating and regulation
523 of connexin 43 (Cx43) hemichannels. *Proc Natl Acad Sci U S A*.
524 2003;100(20):11388-93.
- 525 7. Freitas-Andrade M, Wang N, Bechberger JF, De Bock M, Lampe PD, Leybaert L,
526 et al. Targeting MAPK phosphorylation of Connexin43 provides neuroprotection in
527 stroke. *J Exp Med*. 2019;216(4):916-35.

- 528 8. Gadicherla AK, Wang N, Bulic M, Agullo-Pascual E, Lissoni A, De Smet M, et al.
529 Mitochondrial Cx43 hemichannels contribute to mitochondrial calcium entry and
530 cell death in the heart. *Basic Res Cardiol.* 2017;112(3):27.
- 531 9. Meunier C, Wang N, Yi C, Dallerac G, Ezan P, Koulakoff A, et al. Contribution of
532 Astroglial Cx43 Hemichannels to the Modulation of Glutamatergic Currents by D-
533 Serine in the Mouse Prefrontal Cortex. *J Neurosci.* 2017;37(37):9064-75.
- 534 10. Gilbert G, Demydenko K, Dries E, Puertas RD, Jin X, Sipido K, et al. Calcium
535 Signaling in Cardiomyocyte Function. *Cold Spring Harb Perspect Biol.*
536 2019:a035428.
- 537 11. Antoons G, Willems R, and Sipido KR. Alternative strategies in arrhythmia
538 therapy: evaluation of Na/Ca exchange as an anti-arrhythmic target. *Pharmacol*
539 *Ther.* 2012;134(1):26-42.
- 540 12. Landstrom AP, Dobrev D, and Wehrens XHT. Calcium Signaling and Cardiac
541 Arrhythmias. *Circ Res.* 2017;120(12):1969-93.
- 542 13. Sipido KR, Bito V, Antoons G, Volders PG, and Vos MA. Na/Ca exchange and
543 cardiac ventricular arrhythmias. *Ann N Y Acad Sci.* 2007;1099:339-48.
- 544 14. Leybaert L, Lampe PD, Dhein S, Kwak BR, Ferdinandy P, Beyer EC, et al.
545 Connexins in Cardiovascular and Neurovascular Health and Disease:
546 Pharmacological Implications. *Pharmacol Rev.* 2017;69(4):396-478.
- 547 15. Lillo MA, Himelman E, Shirokova N, Xie L-H, Fraidenraich D, and Contreras JE.
548 S-nitrosylation of Connexin43 hemichannels elicits cardiac stress induced
549 arrhythmias in Duchenne Muscular Dystrophy mice. *JCI Insight.*
550 2019;4(24):e130091.

- 551 16. Patrick Gonzalez J, Ramachandran J, Xie LH, Contreras JE, and Fraidenaich D.
552 Selective Connexin43 Inhibition Prevents Isoproterenol-Induced Arrhythmias and
553 Lethality in Muscular Dystrophy Mice. *Sci Rep.* 2015;5:13490.
- 554 17. Ghazizadeh Z, Kiviniemi T, Olafsson S, Plotnick D, Beerens ME, Zhang K, et al.
555 Metastable Atrial State Underlies the Primary Genetic Substrate for MYL4
556 Mutation-Associated Atrial Fibrillation. *Circulation.* 2020;141(4):301-12.
- 557 18. Kim J-C, Pérez-Hernández M, Alvarado FJ, Maurya SR, Montnach J, Yin Y, et al.
558 Disruption of Ca^{2+}_i Homeostasis and Connexin 43 Hemichannel Function in the
559 Right Ventricle Precedes Overt Arrhythmogenic Cardiomyopathy in Plakophilin-2–
560 Deficient Mice. *Circulation.* 2019;140(12):1015-30.
- 561 19. Murayama T, Ogawa H, Kurebayashi N, Ohno S, Horie M, and Sakurai T. A
562 tryptophan residue in the caffeine-binding site of the ryanodine receptor regulates
563 Ca^{2+} sensitivity. *Commun Biol.* 2018;1(1):98.
- 564 20. Eisner DA, Caldwell JL, Kistamás K, and Trafford AW. Calcium and Excitation-
565 Contraction Coupling in the Heart. *Circ Res.* 2017;121(2):181-95.
- 566 21. Lissoni A, Hulpiau P, Martins-Marques T, Wang N, Bultynck G, Schulz R, et al.
567 RyR2 regulates Cx43 hemichannel intracellular Ca^{2+} -dependent activation in
568 cardiomyocytes. *Cardiovasc Res.* 2021;117(1):123-136.
- 569 22. Trafford AW, Díaz ME, O'Neill SC, and Eisner DA. Comparison of
570 subsarcolemmal and bulk calcium concentration during spontaneous calcium
571 release in rat ventricular myocytes. *J Physiol.* 1995;488(3):577-86.
- 572 23. Weber CR, Piacentino V, Ginsburg KS, Houser SR, and Bers DM. Na^+ - Ca^{2+}
573 exchange current and submembrane $[Ca^{2+}]$ during the cardiac action potential.
574 *Circ Res.* 2002;90(2):182-9.

- 575 24. De Bock M, Wang N, Bol M, Decrock E, Ponsaerts R, Bultynck G, et al. Connexin
576 43 hemichannels contribute to cytoplasmic Ca²⁺ oscillations by providing a
577 bimodal Ca²⁺-dependent Ca²⁺ entry pathway. *J Biol Chem.* 2012;287(15):12250-
578 66.
- 579 25. Kienitz M-C, Bender K, Dermietzel R, Pott L, and Zoidl G. Pannexin 1 constitutes
580 the large conductance cation channel of cardiac myocytes. *J Biol Chem.*
581 2011;286(1):290-8.
- 582 26. Volk T, Schwoerer AP, Thiessen S, Schultz J-H, and Ehmke H. A polycystin-2-
583 like large conductance cation channel in rat left ventricular myocytes. *Cardiovasc*
584 *Res.* 2003;58(1):76-88.
- 585 27. Bermudez-Hernandez K, Keegan S, Whelan DR, Reid DA, Zagelbaum J, Yin Y,
586 et al. A Method for Quantifying Molecular Interactions Using Stochastic Modelling
587 and Super-Resolution Microscopy. *Sci Rep.* 2017;7(1):14882.
- 588 28. Jayasinghe ID, Cannell MB, and Soeller C. Organization of ryanodine receptors,
589 transverse tubules, and sodium-calcium exchanger in rat myocytes. *Biophys J.*
590 2009;97(10):2664-73.
- 591 29. Shen X, van den Brink J, Hou Y, Colli D, Le C, Kolstad TR, et al. 3D dSTORM
592 imaging reveals novel detail of ryanodine receptor localization in rat cardiac
593 myocytes. *J Physiol.* 2019;597(2):399-418.
- 594 30. Macquaide N, Tuan HTM, Hotta JI, Sempels W, Lenaerts I, Holemans P, et al.
595 Ryanodine receptor cluster fragmentation and redistribution in persistent atrial
596 fibrillation enhance calcium release. *Cardiovasc Res.* 2015;108(3):387-98.
- 597 31. Veeraraghavan R, and Gourdie RG. Stochastic optical reconstruction
598 microscopy-based relative localization analysis (STORM-RLA) for quantitative

- 599 nanoscale assessment of spatial protein organization. *Mol Biol Cell*.
600 2016;27(22):3583-90.
- 601 32. Veeraraghavan R, Hoeker GS, Laviada AA, Hoagland D, Wan X, King DR, et al.
602 The adhesion function of the sodium channel beta subunit (β 1) contributes to
603 cardiac action potential propagation. *Elife*. 2018;7:e37610.
- 604 33. Rhett JM, and Gourdie RG. The perinexus: A new feature of Cx43 gap junction
605 organization. *Heart Rhythm*. 2012;9(4):619-23.
- 606 34. Rhett JM, Ongstad EL, Jourdan J, and Gourdie RG. Cx43 associates with Nav1.5
607 in the cardiomyocyte perinexus. *J Membr Biol*. 2012;245(7):411-22.
- 608 35. Unger VM, Kumar NM, Gilula NB, and Yeager M. Three-dimensional structure of
609 a recombinant gap junction membrane channel. *Science*. 1999;283(5405):1176-
610 80.
- 611 36. Page E, Karrison T, and Upshaw-Earley J. Freeze-fractured cardiac gap
612 junctions: structural analysis by three methods. *Am J Physiol*. 1983;244(4):H525-
613 39.
- 614 37. Rhett JM, Jourdan J, and Gourdie RG. Connexin 43 connexon to gap junction
615 transition is regulated by zonula occludens-1. *Mol Biol Cell*. 2011;22(9):1516-28.
- 616 38. Lin X, Liu N, Lu J, Zhang J, Anumonwo JMB, Isom LL, et al. Subcellular
617 heterogeneity of sodium current properties in adult cardiac ventricular myocytes.
618 *Heart Rhythm*. 2011;8(12):1923-30.
- 619 39. Jiang D, Xiao B, Yang D, Wang R, Choi P, Zhang L, et al. RyR2 mutations linked
620 to ventricular tachycardia and sudden death reduce the threshold for store-
621 overload-induced Ca^{2+} release (SOICR). *Proc Natl Acad Sci U S A*.
622 2004;101(35):13062-7.

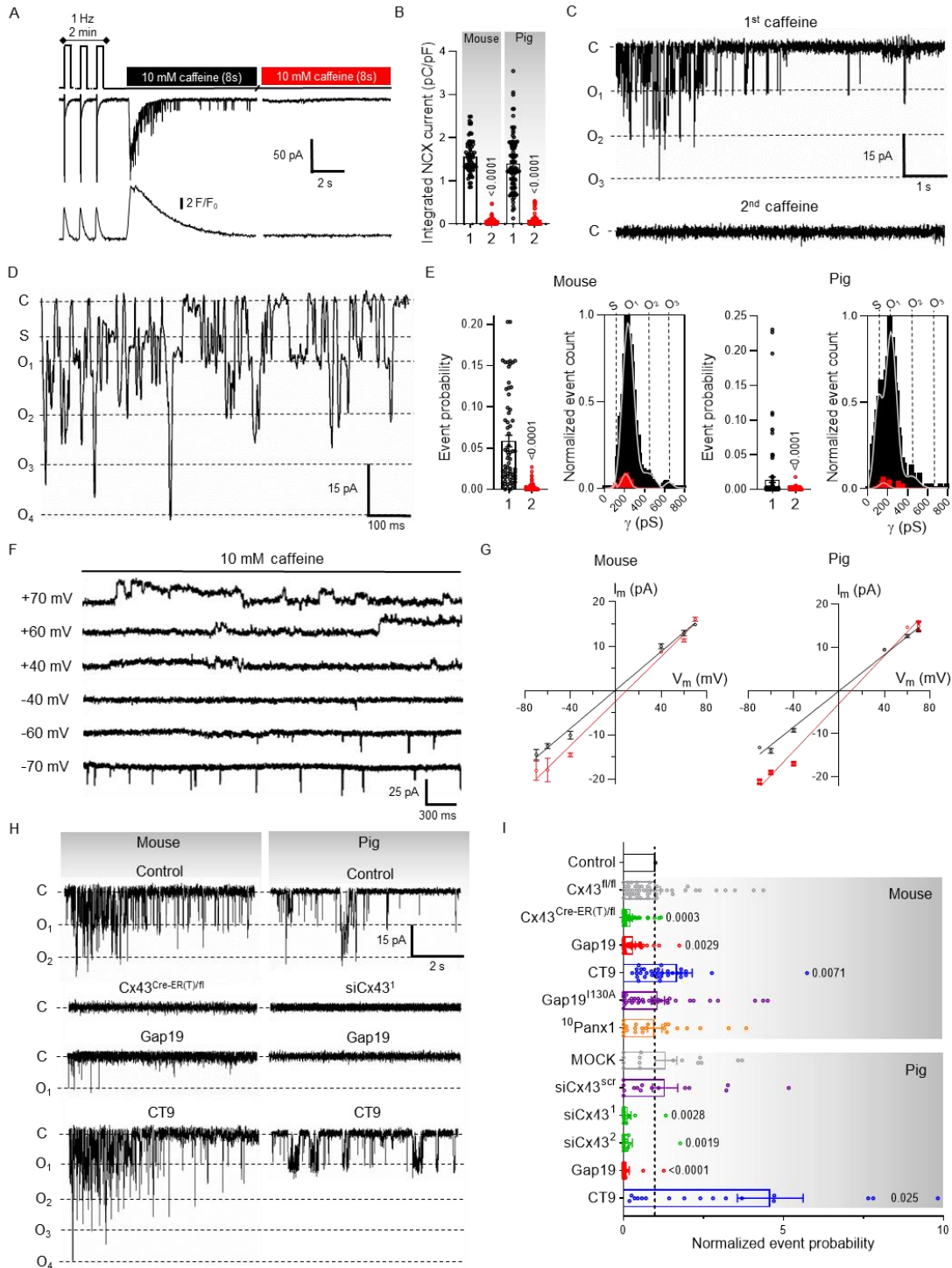
- 623 40. Dibb KM, Eisner DA, and Trafford AW. Regulation of systolic $[Ca^{2+}]_i$ and cellular
624 Ca^{2+} flux balance in rat ventricular myocytes by SR Ca^{2+} , L-type Ca^{2+} current and
625 diastolic $[Ca^{2+}]_i$. *J Physiol*. 2007;585(2):579-92.
- 626 41. Sankaranarayanan R, Kistamás K, Greensmith DJ, Venetucci LA, and Eisner DA.
627 Systolic $[Ca^{2+}]_i$ regulates diastolic levels in rat ventricular myocytes. *J Physiol*.
628 2017;595(16):5545-55.
- 629 42. Sipido KR, Maes M, and Van de Werf F. Low Efficiency of Ca^{2+} Entry Through the
630 Na^+ - Ca^{2+} Exchanger as Trigger for Ca^{2+} Release From the Sarcoplasmic
631 Reticulum. *Circ Res*. 1997;81(6):1034-44.
- 632 43. Trafford AW, Díaz ME, Sibbring GC, and Eisner DA. Modulation of CICR has no
633 maintained effect on systolic Ca^{2+} : Simultaneous measurements of sarcoplasmic
634 reticulum and sarcolemmal Ca^{2+} fluxes in rat ventricular myocytes. *J Physiol*.
635 2000;522(2):259-70.
- 636 44. Venetucci LA, Trafford AW, Díaz ME, O'Neill SC, and Eisner DA. Reducing
637 ryanodine receptor open probability as a means to abolish spontaneous Ca^{2+}
638 release and increase Ca^{2+} transient amplitude in adult ventricular myocytes. *Circ*
639 *Res*. 2006;98(10):1299-305.
- 640 45. Cannell MB, and Soeller C. Numerical analysis of ryanodine receptor activation
641 by L-type channel activity in the cardiac muscle diad. *Biophys J*. 1997;73(1):112-
642 22.
- 643 46. Tao T, O'Neill SC, Diaz ME, Li YT, Eisner DA, and Zhang H. Alternans of cardiac
644 calcium cycling in a cluster of ryanodine receptors: A simulation study. *Am J*
645 *Physiol Heart Circ Physiol*. 2008;295(2):H598-H609.

- 646 47. Pott L, and Mechmann S. Large-conductance ion channel measured by whole-
647 cell voltage clamp in single cardiac cells: modulation by beta-adrenergic
648 stimulation and inhibition by octanol. *J Membr Biol.* 1990;117(2):189-99.
- 649 48. Kondo RP, Weiss JN, and Goldhaber JI. Putative ryanodine receptors in the
650 sarcolemma of ventricular myocytes. *Pflugers Arch.* 2000;440(1):125-31.
- 651 49. Zhang YA, Tuft RA, Lifshitz LM, Fogarty KE, Singer JJ, and Zou H. Caffeine-
652 activated large-conductance plasma membrane cation channels in cardiac
653 myocytes: Characteristics and significance. *Am J Physiol Heart Circ Physiol.*
654 2007;293(4):H2448-61.
- 655 50. Hagen A, Dietze A, and Dhein S. Human cardiac gap-junction coupling: Effects of
656 antiarrhythmic peptide AAP10. *Cardiovasc Res.* 2009;83(2):405-15.
- 657 51. Li Y, Eisner DA, and O'Neill SC. Do calcium waves propagate between cells and
658 synchronize alternating calcium release in rat ventricular myocytes? *J Physiol.*
659 2012;590(24):6353-61.
- 660 52. Dries E, Bito V, Lenaerts I, Antoons G, Sipido KR, and Macquaide N. Selective
661 modulation of coupled ryanodine receptors during microdomain activation of
662 calcium/calmodulin-dependent kinase II in the dyadic cleft. *Circ Res.*
663 2013;113(11):1242-52.
- 664 53. Dries E, Santiago DJ, Johnson DM, Gilbert G, Holemans P, Korte SM, et al.
665 Calcium/calmodulin-dependent kinase II and nitric oxide synthase 1-dependent
666 modulation of ryanodine receptors during β -adrenergic stimulation is restricted to
667 the dyadic cleft. *J Physiol.* 2016;594(20):5923-39.

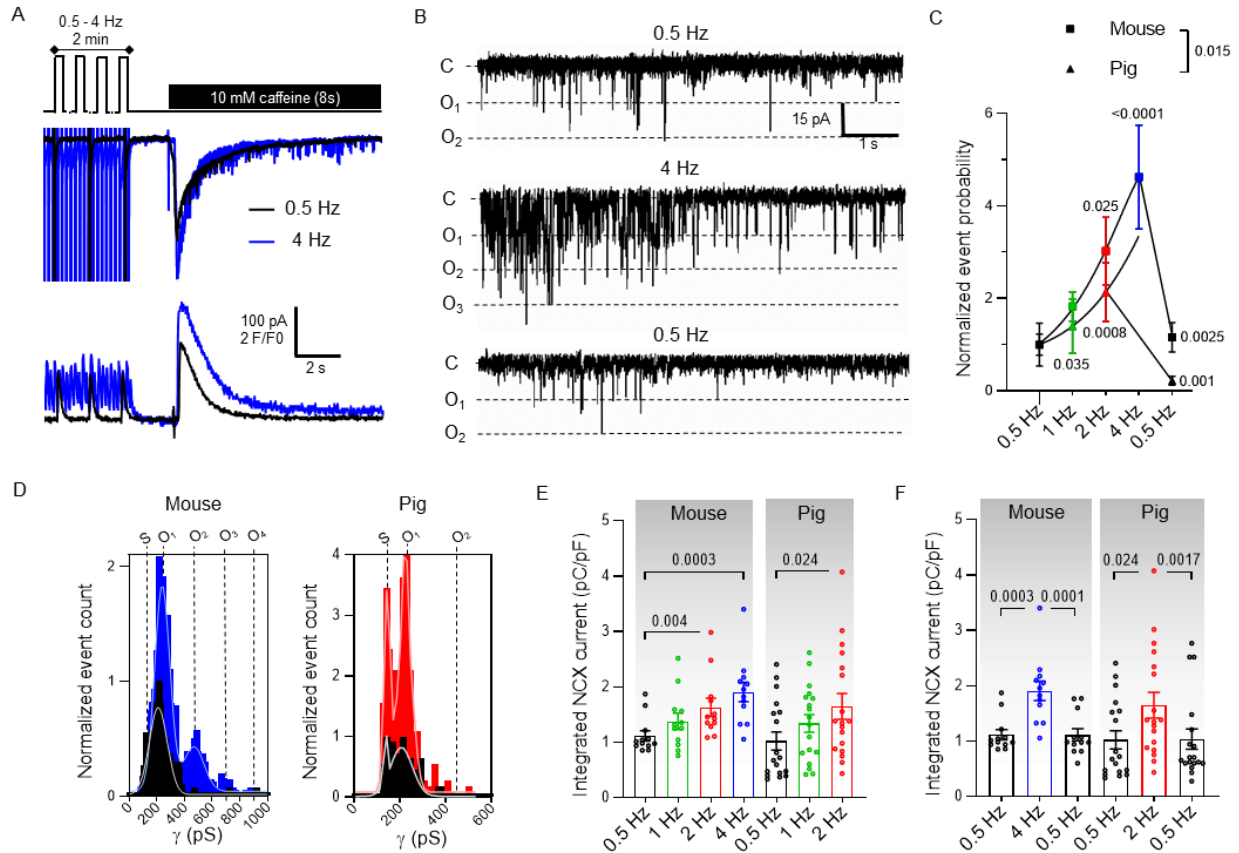
- 668 54. Bennett PM, Ehler E, and Wilson AJ. Sarcoplasmic reticulum is an intermediary of
669 mitochondrial and myofibrillar growth at the intercalated disc. *J Muscle Res Cell*
670 *Motil.* 2016;37(3):55-69.
- 671 55. Leo-Macías A, Liang F-X, and Delmar M. Ultrastructure of the intercellular space
672 in adult murine ventricle revealed by quantitative tomographic electron
673 microscopy. *Cardiovasc Res.* 2015;107(4):442-52.
- 674 56. Himelman E, Lillo MA, Nouet J, Gonzalez JP, Zhao Q, Xie L-H, et al. Prevention
675 of Connexin43 remodeling protects against duchenne muscular dystrophy
676 cardiomyopathy. *J Clin Invest.* 2020;130(4):1713-1727.
- 677 57. Boengler K, Ruiz-Meana M, Gent S, Ungefug E, Soetkamp D, Miro-Casas E, et
678 al. Mitochondrial connexin 43 impacts on respiratory complex i activity and
679 mitochondrial oxygen consumption. *J Cell Mol Med.* 2012;16(8):1649-55.
- 680 58. Boengler K, Ungefug E, Heusch G, Leybaert L, and Schulz R. Connexin 43
681 impacts on mitochondrial potassium uptake. *Front Pharmacol.* 2013;4:73.
- 682 59. Eckardt D, Theis M, Degen J, Ott T, Van Rijen HVM, Kirchhoff S, et al. Functional
683 role of connexin43 gap junction channels in adult mouse heart assessed by
684 inducible gene deletion. *J Mol Cell Cardiol.* 2004;36(1):101-10.
- 685 60. Jansen JA, Noorman M, Musa H, Stein M, de Jong S, van der Nagel R, et al.
686 Reduced heterogeneous expression of Cx43 results in decreased Nav1.5
687 expression and reduced sodium current that accounts for arrhythmia vulnerability
688 in conditional Cx43 knockout mice. *Heart Rhythm.* 2012;9(4):600-7.
- 689 61. Jansen JA, Van Veen TAB, De Jong S, Van Der Nagel R, Van Stuijvenberg L,
690 Driessen H, et al. Reduced Cx43 expression triggers increased fibrosis due to
691 enhanced fibroblast activity. *Circ Arrhythm Electrophysiol.* 2012;5(2):380-90.

- 692 62. Stein M, van Veen TAB, Hauer RNW, de Bakker JMT, and van Rijen HVM. A
693 50% reduction of excitability but not of intercellular coupling affects conduction
694 velocity restitution and activation delay in the mouse heart. *PLoS One*.
695 2011;6(6):e20310.
- 696 63. van Rijen HVM, Eckardt D, Degen J, Theis M, Ott T, Willecke K, et al. Slow
697 conduction and enhanced anisotropy increase the propensity for ventricular
698 tachyarrhythmias in adult mice with induced deletion of connexin43. *Circulation*.
699 2004;109(8):1048-55.
- 700

Figures



703 **Figure 1. Caffeine-induced Ca^{2+} release from the sarcoplasmic reticulum activates**
704 **Cx43 hemichannels at resting membrane potential.**
705 (A) Freshly isolated left ventricular cardiomyocytes were studied under voltage clamp
706 with continuous $[\text{Ca}^{2+}]_i$ recording. Top trace shows experimental protocol. Middle and
707 bottom traces depict current and $[\text{Ca}^{2+}]_i$ signals recorded in mouse.
708 (B) Summary data illustrating abolished NCX current during second caffeine pulse as
709 compared to first pulse (nested t-test), indicating depleted SR Ca^{2+} stores ($N/n_{\text{mouse}} =$
710 $90/281$, $N/n_{\text{pig}} = 20/55$).
711 (C) Unitary current example traces during first and second caffeine applications with
712 NCX current subtracted. 'C' indicates closed state; O_1 corresponds to fully open state
713 while O_2 and O_3 indicate multiples of fully open state.
714 (D) Expanded trace of unitary current activity. 'S' indicates substate.
715 (E) Summary dot plots and transition histograms indicate significantly reduced unitary
716 current event probability during the second caffeine pulse (red) as compared to the first
717 application (black) (nested t-test; $N/n_{\text{mouse}} = 90/281$, $N/n_{\text{pig}} = 20/55$).
718 (F) Unitary current example traces during caffeine application at different membrane
719 voltages. Recordings under conditions of K^+ channel blockade following 30 seconds of 1
720 Hz pacing.
721 (G) IV plots depicting linear current-voltage relationship with slope conductance ~ 220 pS
722 and $E_{\text{rev}} \approx 0$ mV (black line; $N/n_{\text{mouse}} = 5/20$, $N/n_{\text{pig}} = 5/15$). A 5-fold elevation of $[\text{Ca}^{2+}]_e$
723 shifted E_{rev} from 0 to ~ 9.5 mV (red line; $N/n_{\text{mouse}} = 5/20$, $N/n_{\text{pig}} = 5/15$).
724 (H) Unitary current example traces under control conditions and following Cx43
725 knockdown or application of Gap19 or CT9.
726 (I) Summary data of Ca^{2+} release induced unitary current event probability under
727 conditions of Cx43 knockdown or in the presence of Gap19, inactive Gap19^{130A}, CT9 or
728 ¹⁰Panx1 ($N/n_{\text{mouse}} = 5-16/20-49$ per condition, $N/n_{\text{pig}} = 5-6/15-21$ per condition). P-values
729 indicate significance compared to control (nested one-way ANOVA).
730



731

732 **Figure 2. Cx43 hemichannel activation is frequency dependent**

733 (A) Top trace shows experimental protocol: cells were paced for 2 min to steady-state
 734 (mouse 0.5, 1, 2 or 4 Hz; pig 0.5, 1 or 2 Hz) followed by caffeine superfusion. Middle and
 735 bottom traces depict current and $[Ca^{2+}]_i$ signals recorded in mouse following 0.5 (black)
 736 or 4 Hz (blue) pacing.

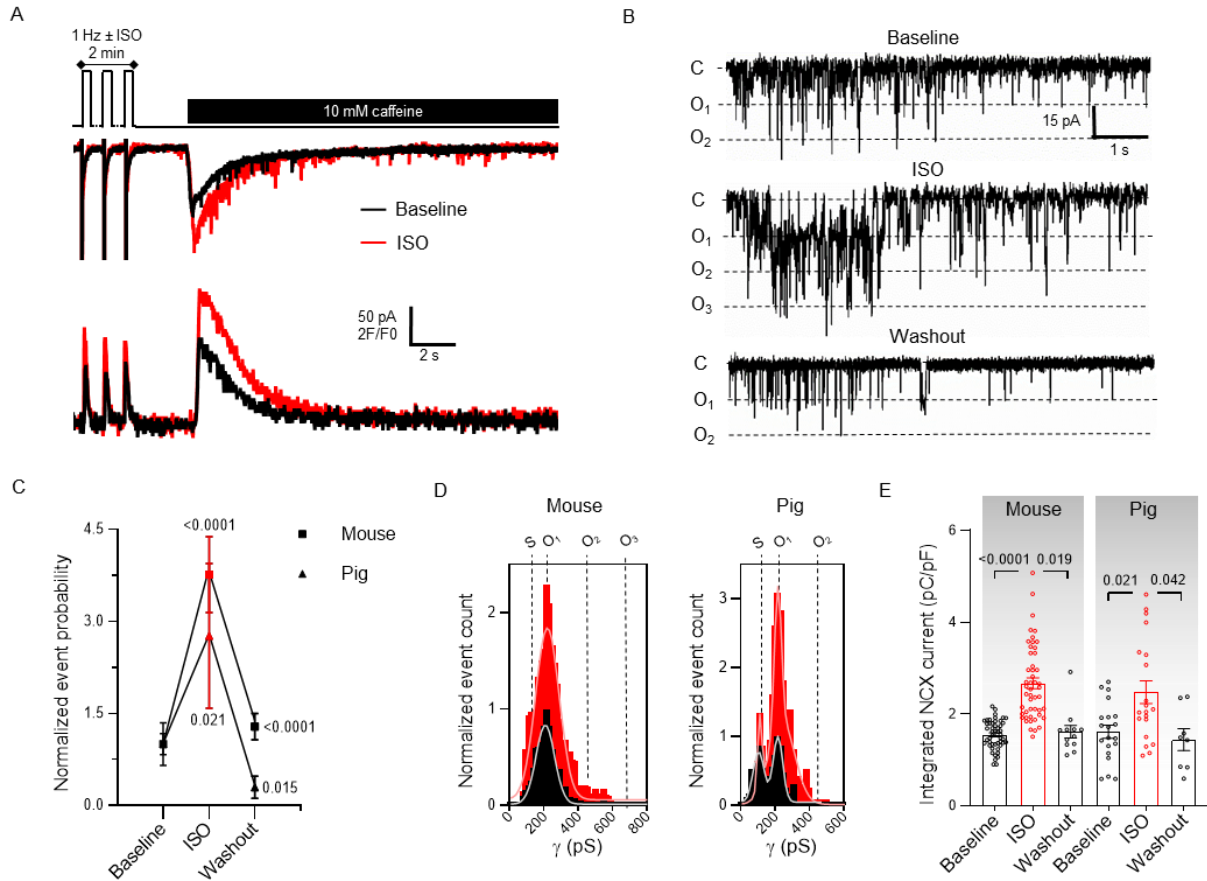
737 (B) Unitary current example traces following 0.5 and 4 Hz including reversibility (NCX
 738 currents subtracted).

739 (C) and (D) Summary graph and transition histograms indicate significant and reversible
 740 increase in unitary current event probability with increasing pacing frequency ($N/n_{mouse} =$
 741 $4/12$, $N/n_{pig} = 7/19$). P-values compare to 0.5 Hz or to 2/4 Hz (nested one-way ANOVA).

742 (E) Summary dot plot depicting significant increase in SR Ca^{2+} content with increasing
 743 frequency, as determined by integrating NCX current during caffeine (nested one-way
 744 ANOVA; $N/n_{mouse} = 4/12$, $N/n_{pig} = 7/19$).

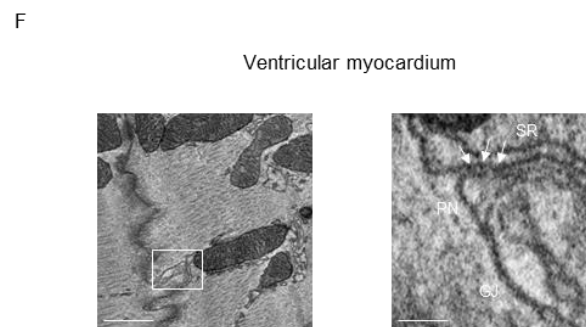
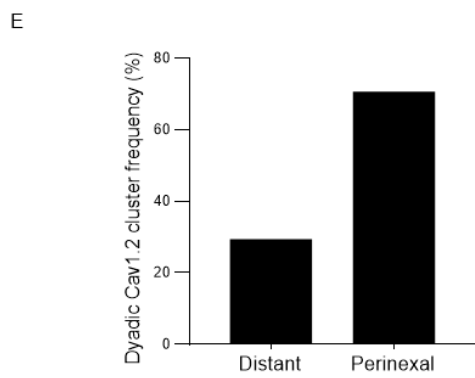
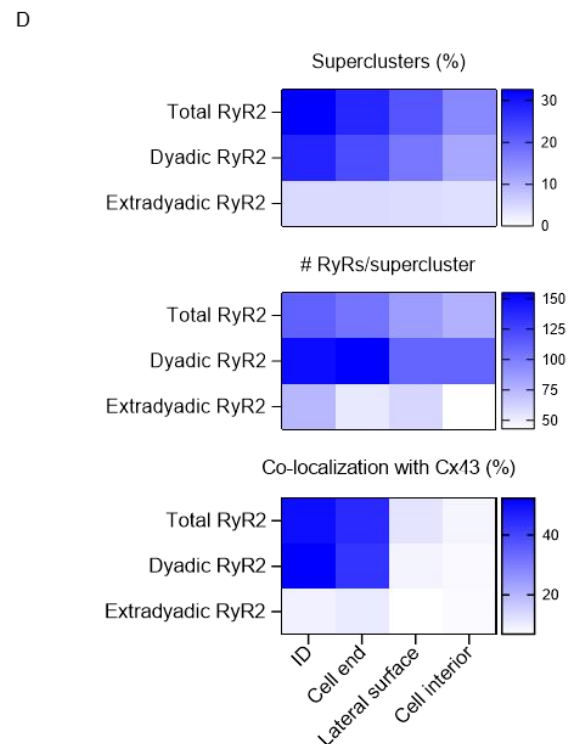
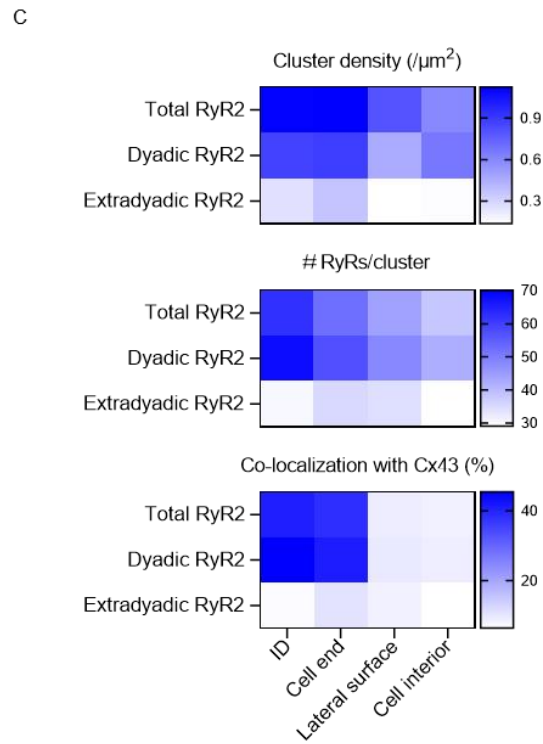
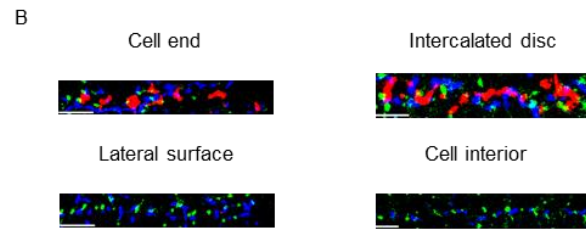
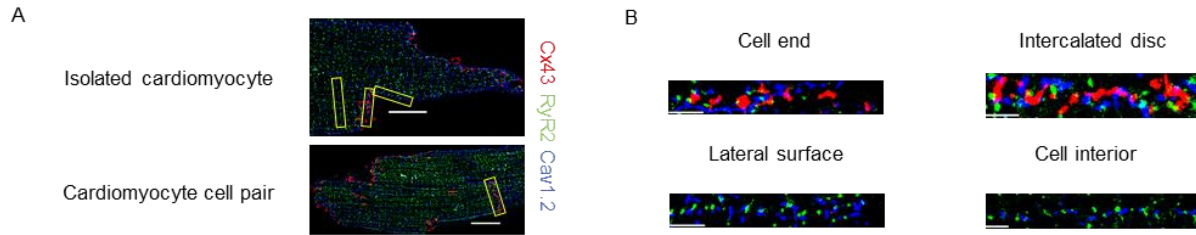
745 (F) Summary dot plot depicting reversible increase in SR Ca^{2+} content with increasing
 746 frequency (nested one-way ANOVA; $N/n_{mouse} = 4/12$, $N/n_{pig} = 7/19$).

747



748

749 **Figure 3. Cx43 hemichannel activation is modulated by β -adrenergic stimulation.**
 750 (A) Top trace shows experimental protocol: β -adrenergic stimulation (1 μ mol/L
 751 isoproterenol for mouse; 10 nmol/L pig) was applied when pacing frequency was 1 Hz.
 752 Middle and bottom traces depict current and $[Ca^{2+}]_i$ signals recorded in mouse following
 753 1 Hz pacing without (black) or with isoproterenol (red).
 754 (B) Unitary current example traces in the absence or presence of isoproterenol,
 755 including washout (NCX currents subtracted).
 756 (C) and (D) Summary graph and transition histograms indicate significant and reversible
 757 increase in unitary current event probability with isoproterenol compared to baseline
 758 (nested one-way ANOVA; $N/n_{\text{mouse}} = 20/49$, $N/n_{\text{pig}} = 8/20$).
 759 (D) Summary dot plot illustrating reversible increase in SR Ca^{2+} content with
 760 isoproterenol compared to baseline (nested one-way ANOVA; $N/n_{\text{mouse}} = 20/49$, $N/n_{\text{pig}} =$
 761 $8/20$).

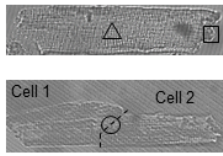


762

763

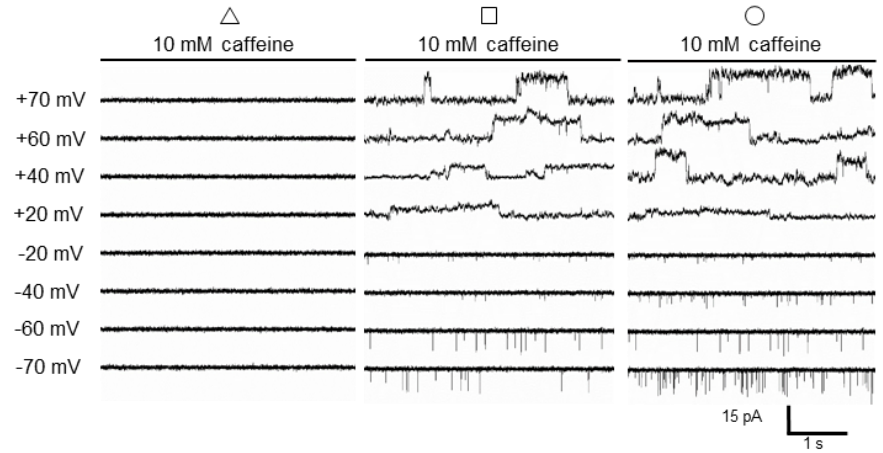
764 **Figure 4. Cx43 co-localizes with large dyadic RyR2 superclusters and forms**
765 **microdomains at the perinexus.**
766 (A) 2D SMLM images of a murine cardiomyocyte (top) and cardiomyocyte cell pair
767 (bottom), triple stained for Cx43 (red), RyR2 (green) and Cav1.2 (blue). Scale bar = 10
768 μm .
769 (B) Straightened region of interests (from yellow boxes in A) of Cx43, RyR2 and Cav1.2
770 at different subcellular domains. Scale bar = 2 μm .
771 (C) Heat map of RyR2 cluster density, number of molecules and co-localization with
772 Cx43 at different subcellular domains (N = 5, n = 42 single cardiomyocytes, 16
773 cardiomyocyte cell pairs). RyR2 clusters were classified as dyadic or extradyadic based
774 on the proximity of Cav1.2 clusters, RyR2 clusters occurring < 250 nm of a Cav1.2
775 clusters were categorized as dyadic.
776 (D) Heat map of RyR2 supercluster abundance, size and co-localization with Cx43 at
777 different subcellular domains (N = 5, n = 42 single cardiomyocytes, 16 cardiomyocyte
778 cell pairs).
779 (E) Relative localization overview in left ventricular mouse cardiomyocyte cell pairs.
780 Dyadic Cav1.2 clusters were categorized as perinexal or distant based on edge distance
781 \leq or $>$ 200 nm from edge of Cx43 cluster respectively (N = 5, n = 16 cardiomyocyte cell
782 pairs).
783 (F) EM images of a SR cistern forming a dyadic cleft at the perinexus in mouse
784 ventricular myocardium. Left image shows an EM overview of a murine ventricular
785 intercalated disc. Scale bar = 500 nm. White box is enlarged on the right. Arrows
786 indicate electron dense particles, likely ryanodine receptors. Scale bar = 100 nm. PN =
787 perinexus.

A

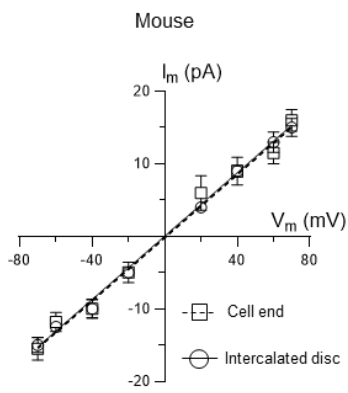


- Cell end
- △ Lateral surface
- Intercalated disc

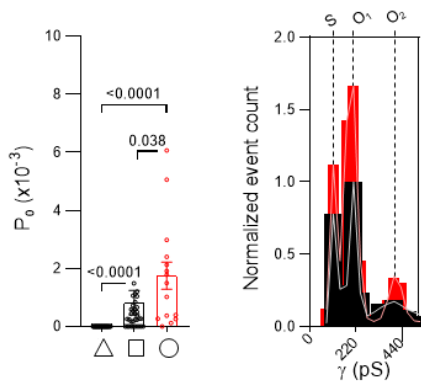
B



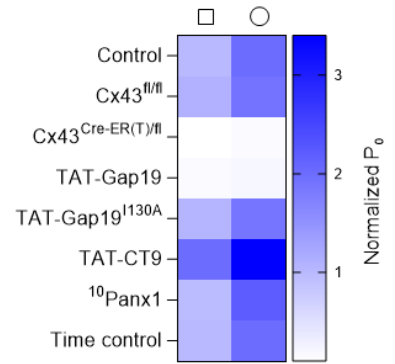
C



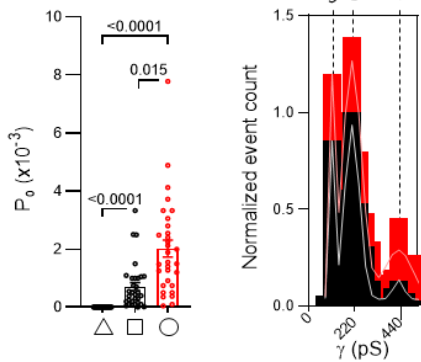
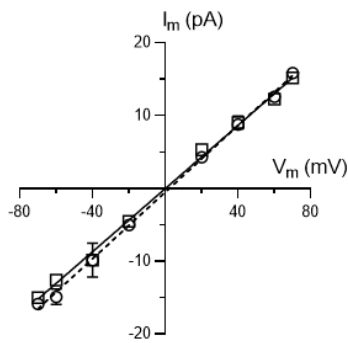
D



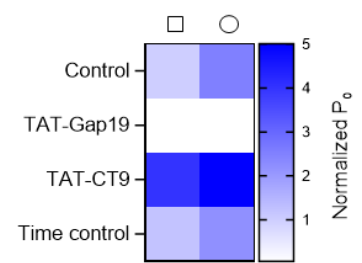
Mouse



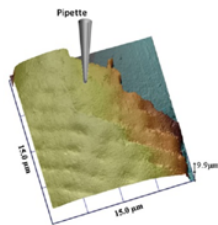
Pig



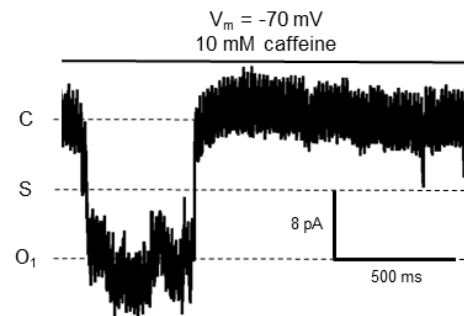
Pig



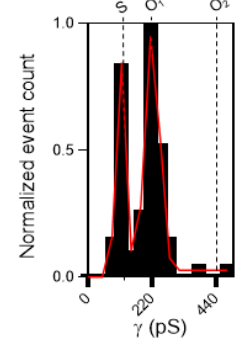
E



F



G



789 **Figure 5. Discrete sites of Cx43 hemichannel activation at the intercalated disc**
790 **during Ca²⁺ release from the sarcoplasmic reticulum.**
791 (A) Transmitted light images of a single cardiomyocyte (top) and cardiomyocyte cell pair
792 (bottom). Triangle, square and circle symbols indicate cell-attached macropatch ($R_p = \sim 2$
793 M Ω , ~ 2 μm pipette inner diameter) recording positions at the lateral membrane and cell
794 end of single cardiomyocytes and intercalated disc of cardiomyocyte cell pairs
795 respectively.
796 (B) Example traces showing single channel currents recorded at the lateral membrane,
797 cell end or intercalated disc. Traces recorded in mouse cardiomyocytes during caffeine
798 superfusion (10 mM, 8 s) at indicated membrane potentials.
799 (C) IV plots depicting linear current-voltage relationship with slope conductance of ~ 220
800 pS and $E_{\text{rev}} \approx 0$ mV ($N/n_{\text{mouse}} = 5/10-18$ patches per conditions, $N/n_{\text{pig}} = 5/15-20$ patches
801 per condition).
802 (D) Summary dot plots and transition histograms indicate recording of ~ 220 pS single
803 channel currents at the cell end of single cardiomyocytes, but not at the lateral
804 membrane, with significantly increased open probability at the intercalated disc of
805 cardiomyocyte cell pairs. Comparative statistics with nested one-way ANOVA. Heat map
806 summarizes single channel open probability at the cell end or at the intercalated disc
807 under conditions of Cx43 knockdown or in the presence of TAT-Gap19, inactive TAT-
808 Gap19^{130A}, TAT-CT9 or ¹⁰Panx1 ($N/n_{\text{mouse}} = 5/10-18$ patches per conditions, $N/n_{\text{pig}} =$
809 $5/15-20$ patches per condition).
810 (E) SICM-generated membrane topology of the cell end of a mouse left ventricular
811 cardiomyocyte. Pipette indicates the recording position distally of the last Z-line.
812 (F) Example trace recorded at -70 mV during caffeine superfusion.
813 (G) Transition histogram from all experiments ($N = 5$, $n = 35$) showing a fully open state
814 at ~ 220 pS and a substate at ~ 110 pS.

816 **Figure 6. Cx43 hemichannel opening during adrenergic stimulation modulates**
817 **spontaneous Ca²⁺ release from the sarcoplasmic reticulum and arrhythmogenic**
818 **afterdepolarizations.**

819 (A) Freshly isolated mouse and pig left ventricular cardiomyocytes were subjected to
820 voltage clamp experiments while [Ca²⁺]_i was simultaneously monitored. Top trace shows
821 experimental protocol: cells were paced to steady-state for 2 min at 1 Hz and then
822 clamped to -70 mV. Middle and bottom traces depict resulting current and [Ca²⁺]_i
823 signals: final three paced Ca²⁺ transients and accompanying currents followed by 15
824 seconds rest period showing spontaneous diastolic Ca²⁺ release with resulting NCX
825 current. Protocols were repeated at 2 Hz with and without isoproterenol. Example traces
826 were recorded in pig.

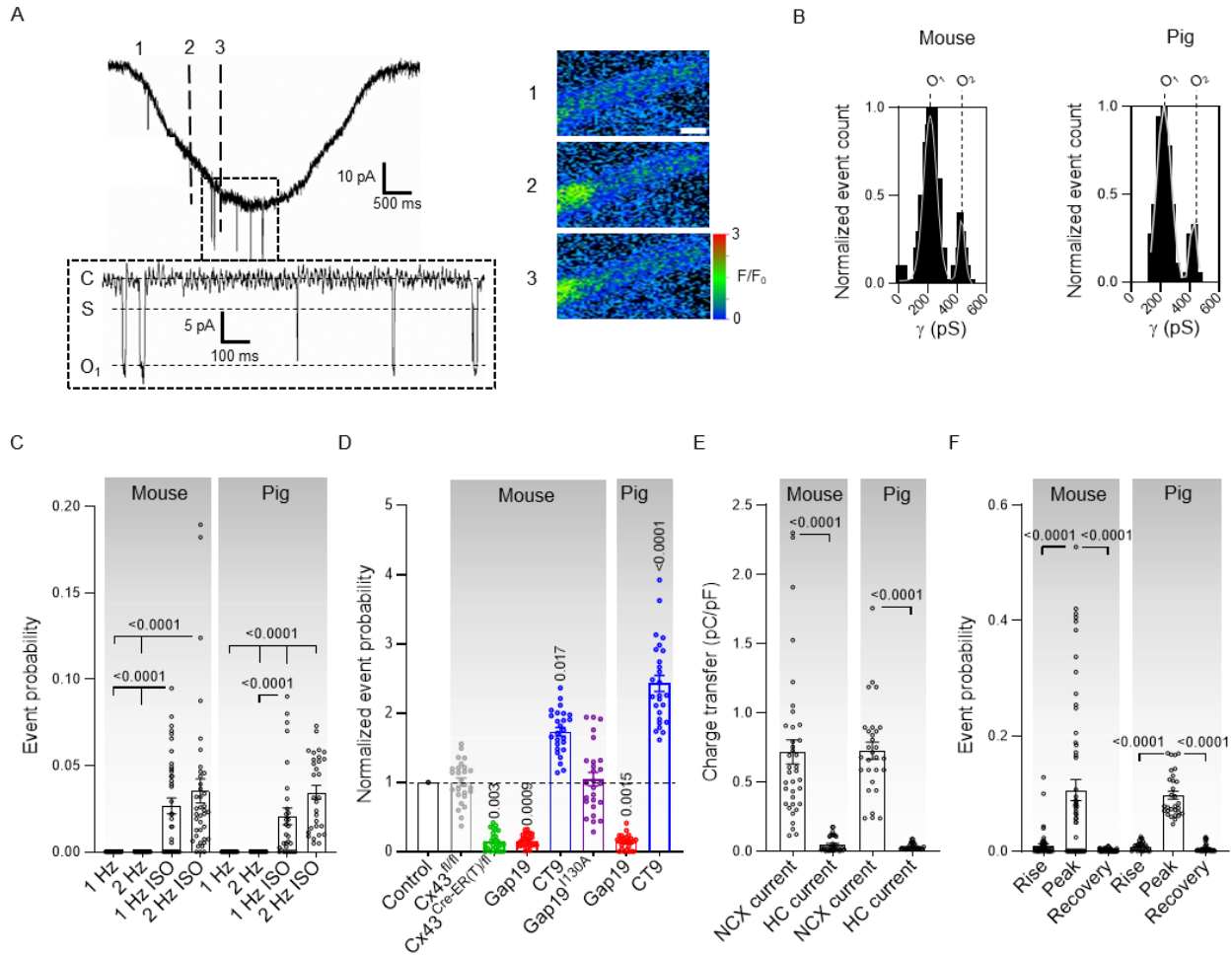
827 (B) In a subset of experiments, we switched to current clamp mode following steady-
828 state pacing in voltage clamp. Example traces, recorded in the same pig cardiomyocyte,
829 without and with TAT-Gap19 recorded in current clamp mode following 2 min pacing to
830 steady-state at 2 Hz with isoproterenol (in voltage clamp mode). Black arrows indicate
831 DADs, red arrow indicates a triggered action potential.

832 (C) Summary dot plots (nested one-way ANOVA; N/n_{mouse} = 23/75 for voltage clamp
833 experiments and N/n_{mouse} = 5/45 for current clamp experiments) illustrating increased
834 frequency and amplitude of diastolic Ca²⁺ release with increased resulting NCX current
835 and membrane depolarization during adrenergic stimulation (2 Hz + ISO) as compared
836 to baseline. tAP = triggered action potential. Similar results were obtained in pig (not
837 shown).

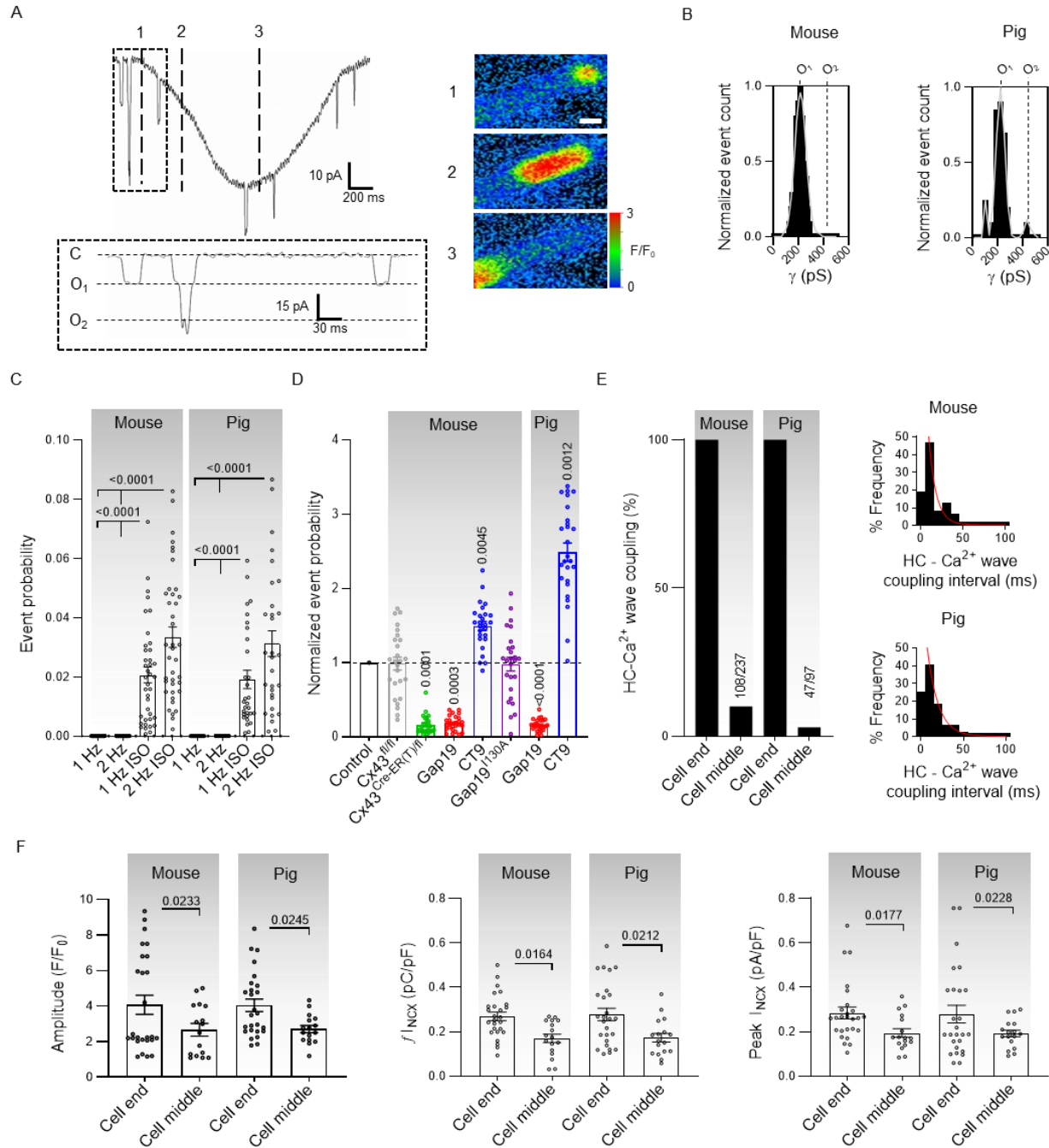
838 (D) Summary data showing the impact of different interventions on diastolic Ca²⁺ release
839 and resulting NCX currents and membrane depolarization (nested one-way ANOVA;
840 N/n_{mouse} = 5-11/15-24 per condition, N/n_{pig} = 5/15-20 per condition). Values reported as
841 differences from the control condition.

842

843



844
 845 **Figure 7. Spontaneous Cx43 hemichannel openings during Ca²⁺ waves**
 846 (A) Left, NCX current during spontaneous Ca²⁺ release with superimposed unitary
 847 currents. Inset shows detail of unitary current activity. Right, Ca²⁺ images corresponding
 848 to time points indicated by dashed lines in left trace. Scale bar = 10 μm.
 849 (B) Transition histograms of superimposed unitary activity showing ~220 pS unitary
 850 conductance (N/n_{mouse} = 23/75, N/n_{pig} = 10/30).
 851 (C) Summary dot plot illustrating increasing unitary current event probability with
 852 increasing pacing frequency and with isoproterenol (nested one-way ANOVA; N/n_{mouse} =
 853 23/75, N/n_{pig} = 10/30).
 854 (D) Summary data showing the effect of different interventions at 2 Hz + ISO (N/n_{mouse} =
 855 5-11/15-24 per condition, N/n_{pig} = 5/15 per condition). P-values indicate significance
 856 compared to control (nested one-way ANOVA).
 857 (E) Summary dot plot depicting relative integrals of NCX and unitary current at 2 Hz +
 858 ISO (nested t-test; N/n_{mouse} = 23/75, N/n_{pig} = 10/30).
 859 (F) Summary dot plot depicting unitary current event probability during different phases
 860 of NCX current induced by spontaneous Ca²⁺ release (nested one-way ANOVA; N/n_{mouse}
 861 = 23/75, N/n_{pig} = 10/30). These phases include the rising phase ('rise', 10-90%), peak
 862 and recovery (90-10%).
 863



864
 865 **Figure 8. Spontaneous Cx43 hemichannel openings preceding Ca²⁺ waves**
 866 **promote arrhythmogenic Ca²⁺ release and resulting depolarizing current.**
 867 (A) Left, unitary currents preceding diastolic Ca²⁺ release. Inset shows detail of unitary
 868 current activity. Right, Ca²⁺ images corresponding to time points indicated by dashed
 869 lines in left trace. Scale bar = 10 μm.
 870 (B) Transition histograms showing ~220 pS unitary conductance of preceding unitary
 871 activity (N/n_{mouse} = 23/75, N/n_{pig} = 10/30).

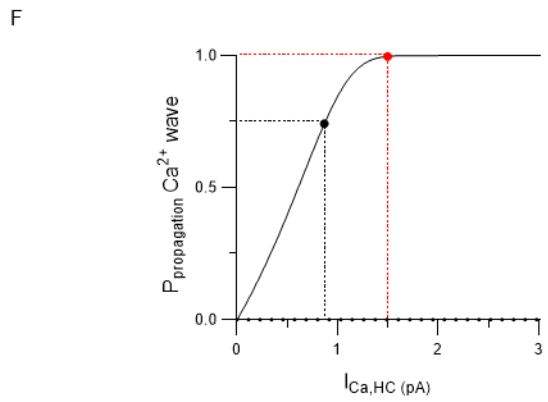
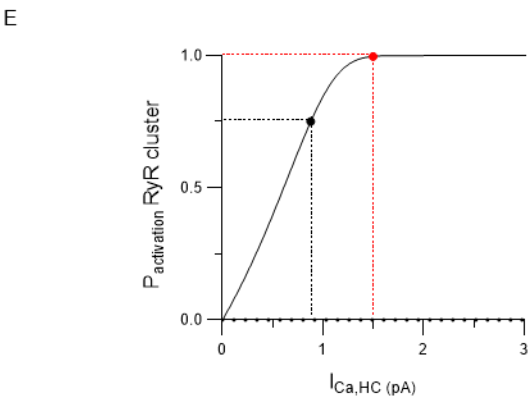
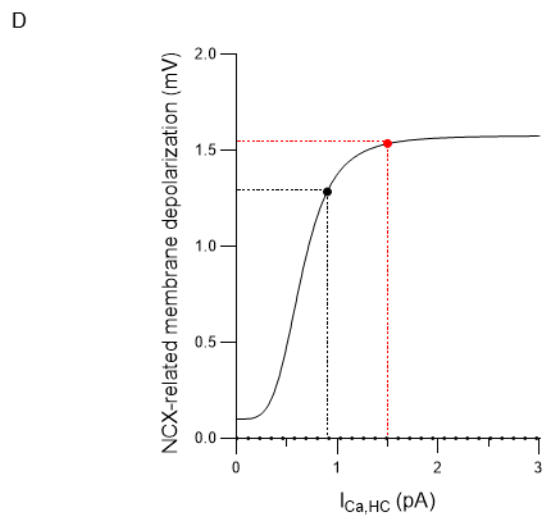
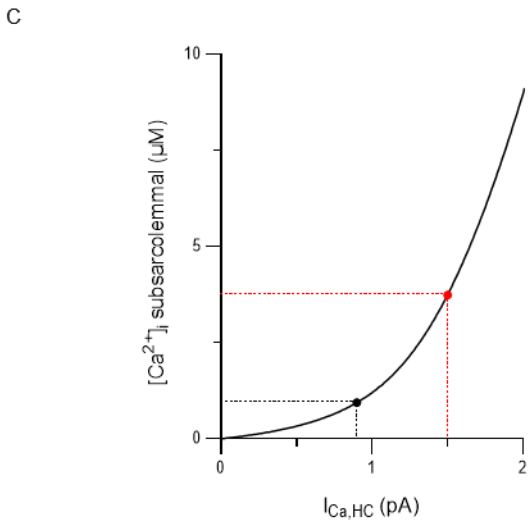
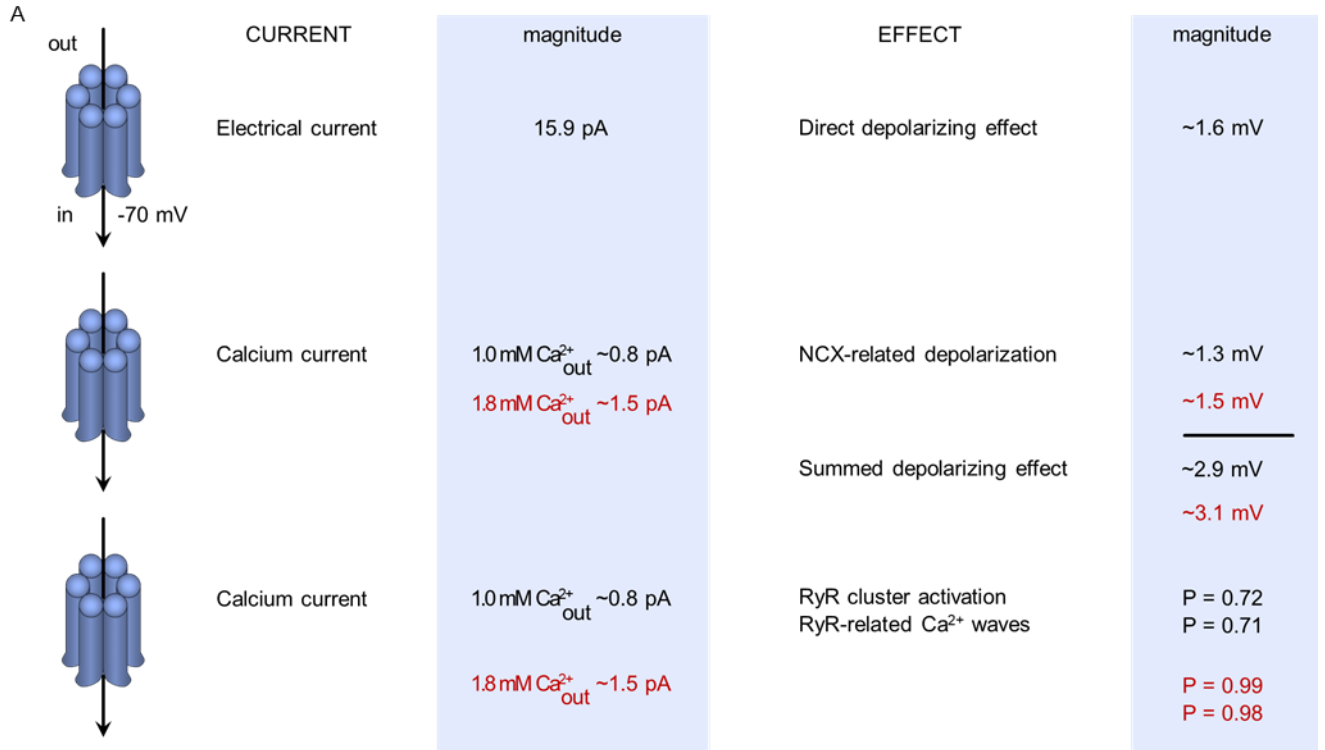
872 (C) Summary dot plot illustrating increasing unitary current event probability with
873 increasing pacing frequency and with isoproterenol (nested one-way ANOVA; $N/n_{\text{mouse}} =$
874 $23/75$, $N/n_{\text{pig}} = 10/30$).

875 (D) Summary data showing the effect of different interventions at 2 Hz + ISO ($N/n_{\text{mouse}} =$
876 $5-11/15-24$ per condition, $N/n_{\text{pig}} = 5/15$ per condition). P-values indicate significance
877 compared to control (nested one-way ANOVA).

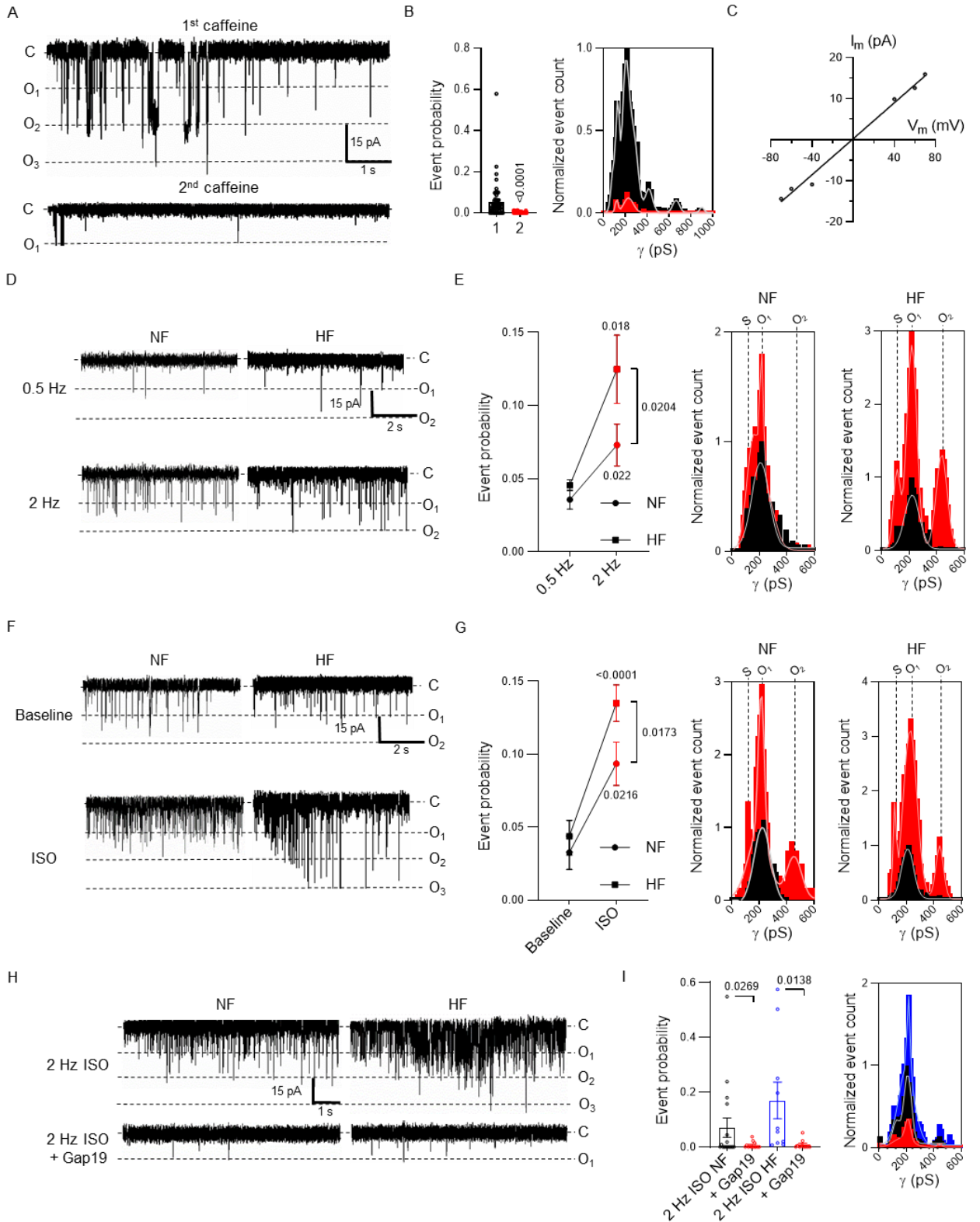
878 (E) Fraction and coupling interval of Cx43 hemichannel (HC)-associated Ca^{2+} release
879 ($N/n_{\text{mouse}} = 23/75$, $N/n_{\text{pig}} = 10/30$). Left graph indicates that HC- Ca^{2+} release coupling to
880 Ca^{2+} waves occurs at the cell end. Numbers show absolute counts. Right histogram
881 indicates time from hemichannel opening to Ca^{2+} release.

882 (F) Dot plots summarizing properties of diastolic Ca^{2+} release and resulting NCX
883 currents categorized by origin (nested t-test; $N/n_{\text{mouse}} = 23/75$, $N/n_{\text{pig}} = 10/30$).

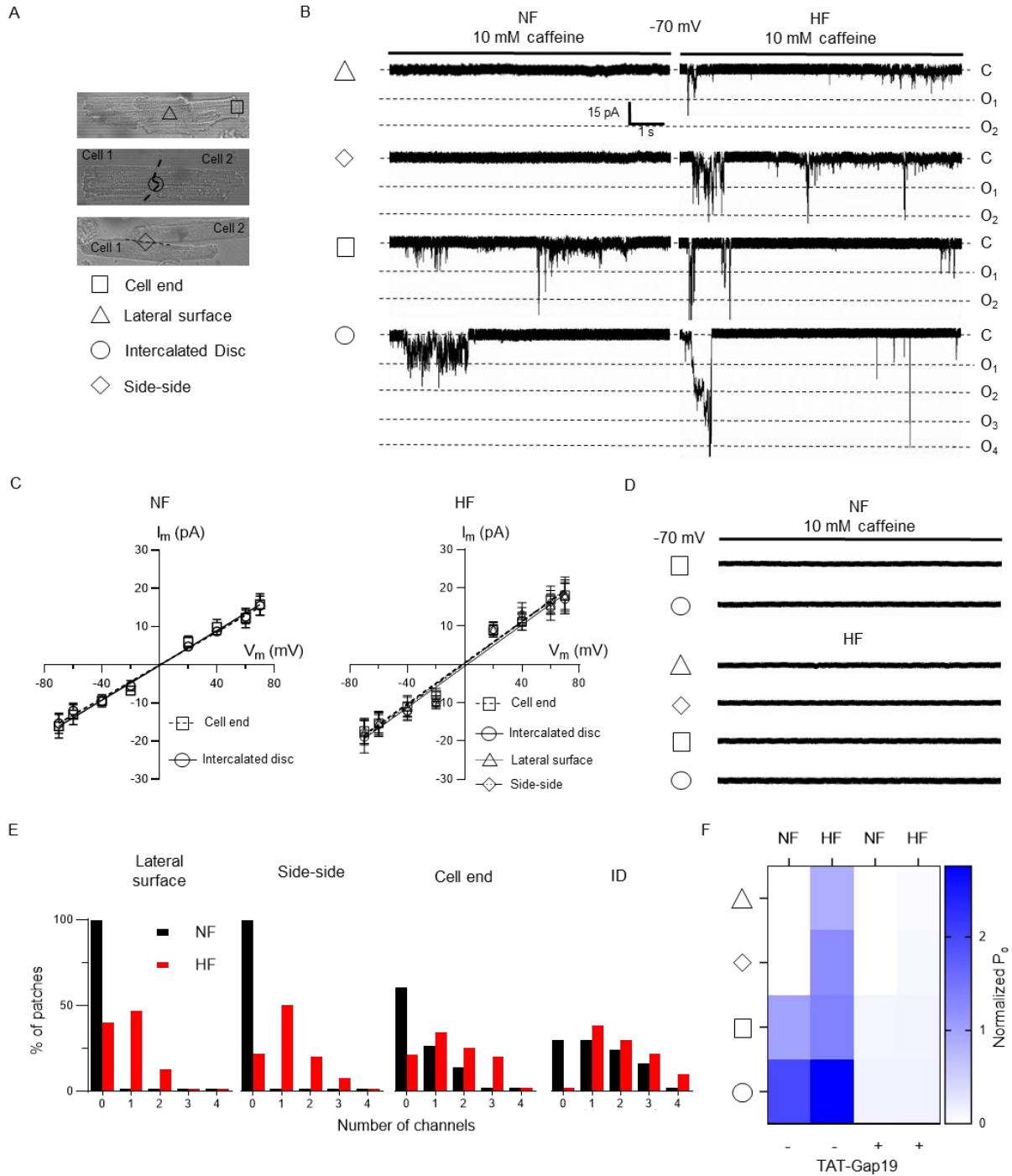
884



886 **Figure 9. Modeling based estimations of electrical and Ca²⁺ consequences of**
887 **single hemichannel opening.**
888 (A) Schematic overview of electrical and Ca²⁺ consequences of single hemichannel
889 opening. The 15.9 pA electrical current is a measured value while the 0.8 pA and 1.5 pA
890 Ca²⁺ currents are calculated estimates using 1.0 and 1.8 mM of extracellular Ca²⁺
891 respectively. Panels B to E further explore the impact of a range of hemichannel Ca²⁺
892 currents. Note that the values given are only valid at -70 mV membrane potential and
893 37°C. Further modeling details can be found in supplemental information.
894 (B) Peak elevation of subsarcolemmal [Ca²⁺]_i as a function of single hemichannel Ca²⁺
895 current (I_{Ca,HC}).
896 (C) Membrane depolarization associated with Ca²⁺ entry associated NCX activation.
897 Black and red points indicate hemichannel Ca²⁺ current estimates, which are close to or
898 in the plateau phase of the curve.
899 (D) Probability of activation of RyR superclusters as a function of single hemichannel
900 Ca²⁺ current.
901 (E) Probability of Ca²⁺ wave propagation as a function of single hemichannel Ca²⁺
902 current.
903



906 **Figure 10. Identification and regulation of Cx43 hemichannels in non-failing and**
907 **failing human ventricular cardiomyocytes.**
908 (A) Unitary current example traces during first and second caffeine applications, NCX
909 current subtracted. Recorded in non-failing left ventricular human cardiomyocyte.
910 (B) Summary dot plot and transition histogram indicating significantly reduced unitary
911 current event probability during the second caffeine pulse (red) as compared to the first
912 (black) (nested t-test; $N/n_{NF} = 20/64$).
913 (C) IV plots depicting linear current-voltage relationship with slope conductance ~ 220 pS
914 and $E_{rev} \approx 0$ mV ($N/n_{NF} = 4/14$).
915 (D) Ca^{2+} release-induced unitary current example traces following 0.5 and 2 Hz pacing
916 in non-failing and failing human cardiac myocytes (NCX currents subtracted).
917 (E) Summary graph and transition histograms indicate significant increase in unitary
918 current event probability with increasing pacing frequency (nested t-test; $N/n_{NF} = 5/25$,
919 $N/n_{HF} = 5/25$). This effect is significantly stronger at 2 Hz in failing as compared to non-
920 failing cardiomyocytes (nested t-test).
921 (F) Ca^{2+} release-induced unitary current example traces in the absence and presence of
922 isoproterenol (10 nmol/L) in non-failing and failing human cardiac myocytes (NCX
923 currents subtracted).
924 (G) Summary graph and transition histograms indicate significant increase in unitary
925 current event probability with isoproterenol as compared to baseline (nested t-test;
926 $N/n_{NF} = 5/13$, $N/n_{HF} = 5/14$). The effect is significantly stronger with ISO in failing as
927 compared to non-failing cardiomyocytes (nested t-test).
928 (H) Ca^{2+} release-induced unitary current example traces during fast pacing and
929 adrenergic stimulation in non-failing and failing human cardiomyocytes. Including Gap19
930 in the pipette solution abolished unitary current activity (NCX currents subtracted).
931 (I) Summary dot plot and transition histogram illustrating increased event probability in
932 failing as compared to non-failing myocytes. Gap19 significantly reduced event
933 probability in non-failing and failing cardiomyocytes (nested one-way ANOVA; $N/n_{NF} =$
934 $4/15$, $N/n_{HF} = 5/15$).
935

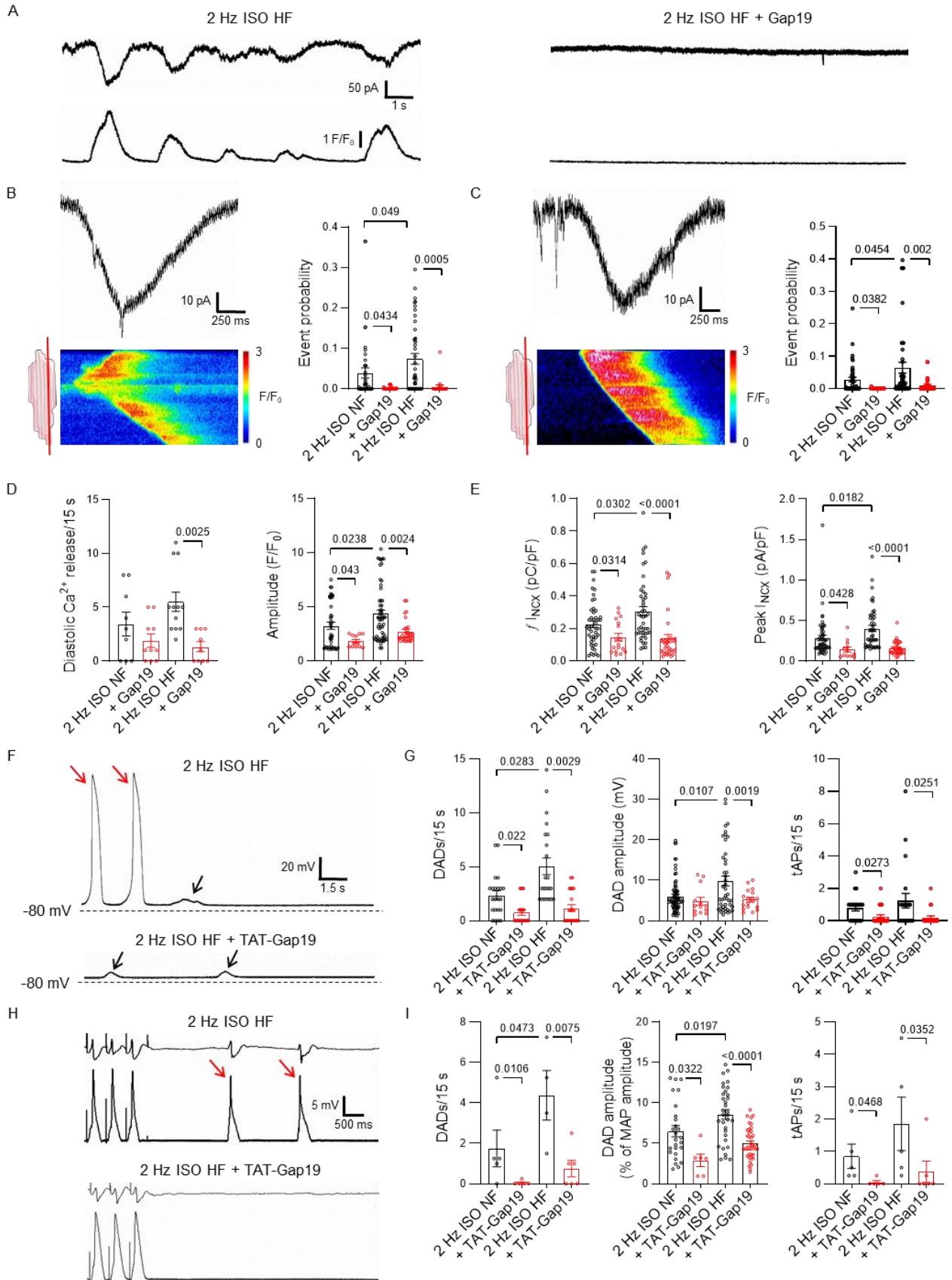


936

937 **Figure 11. Microdomain specific activation of Cx43 hemichannels in non-failing**
 938 **and failing human cardiomyocytes.**

939 (A) Transmitted light images of single cardiomyocyte (top) and cardiomyocyte cell pairs
 940 (middle, bottom). Triangle, square, circle and diamond symbols indicate cell-attached
 941 macropatch positions at the lateral membrane and cell end of single cardiomyocytes,
 942 and intercalated disc and side-side of cardiomyocyte cell pairs respectively.

943 (B) Example traces showing single channel currents recorded at the different
944 macropatch recording positions. Traces recorded in non-failing and failing human
945 cardiomyocytes during caffeine superfusion (10 mM, 8 s) at -70 mV.
946 (C) IV plots depicting linear current-voltage relationship with slope conductance of ~220
947 pS and $E_{rev} \approx 0$ mV ($N/n_{NF} = 3/10-15$ per recording position, $N/n_{HF} = 3/10-15$ per
948 recording position).
949 (D) Example traces showing single channel currents recorded at the different
950 macropatch recording positions following TAT-Gap19 superfusion.
951 (E) Summary histograms depicting number of channels per patch for the different
952 macropatch recording positions ($N/n_{NF} = 3/10-15$ per recording position, $N/n_{HF} = 3/10-15$
953 per recording position). Black and red bars indicate recordings in non-failing and failing
954 human cardiomyocytes respectively.
955 (F) Heat map summarizing single channel open probability at different macropatch
956 recording positions with and without TAT-Gap19 in non-failing and failing human single
957 cardiomyocytes and cardiomyocyte cell pairs ($N/n_{NF} = 3/10-15$ per recording position,
958 $N/n_{HF} = 3/10-15$ per recording position).



960 **Figure 12. Contribution of Cx43 hemichannels to spontaneous Ca²⁺ release and**
961 **afterdepolarizations in human heart failure.**
962 (A) Example traces of spontaneous diastolic Ca²⁺ release and resulting NCX currents
963 recorded in failing human left ventricular cardiomyocytes following fast pacing and
964 adrenergic stimulation with or without Gap19.
965 (B) and (C) unitary current detail and associated confocal line scan images during and
966 preceding spontaneous Ca²⁺ release respectively. Red line on cartoons indicate scan
967 line position. Dot plots show significant increase in unitary current event probability in
968 failing as compared to non-failing cardiomyocytes. Gap19 abolished unitary current
969 activities (nested one-way ANOVA; N/n_{NF} = 5/13, N/n_{HF} = 5/14).
970 (D) and (E) Summary dot plots illustrating increased frequency and significantly
971 increased amplitude of spontaneous Ca²⁺ release and associated NCX currents in
972 human heart failure. Gap19 abolished Ca²⁺ release and NCX currents, especially in
973 heart failure (nested one-way ANOVA; N/n_{NF} = 5/13, N/n_{HF} = 5/14).
974 (F) Example traces of delayed afterdepolarizations and triggered action potentials
975 recorded in a failing human left ventricular cardiomyocytes at baseline and after TAT-
976 Gap19 superfusion. Black arrows indicate DADs, red arrows indicate triggered action
977 potentials.
978 (G) Summary dot plots showing significantly increased frequency and amplitude of
979 DADs and triggered action potential frequency in failing as compared to non-failing
980 cardiac myocytes. TAT-Gap19 abolished DADs and triggered action potentials,
981 especially in human heart failure (nested one-way ANOVA; N/n_{NF} = 6/22, N/n_{HF} = 5/22).
982 (H) Example ECG (top traces) and monophasic action potential traces (lower traces)
983 recorded during adrenergic stimulation (baseline and following TAT-Gap19) in an
984 arterially perfused left ventricular tissue wedge prepared from failing human heart. Red
985 arrows indicate triggered action potentials.
986 (I) Summary dot plots showing significantly increased frequency and amplitude of DADs
987 and triggered action potential frequency in failing as compared to non-failing tissue
988 wedges. TAT-Gap19 abolished DADs and triggered action potentials, especially in
989 human heart failure (nested one-way ANOVA; N/n_{NF} = 5/10, N/n_{HF} = 4/9).